RUPRECHT-KARLS-UNIVERSITÄT HEIDELBERG

Simon Schröder

A measurement of the production cross section of $B_c^{\pm}$ mesons observed through their decay to $J/\psi\pi^{\pm}$, relative to the production cross section of $B^{\pm}$ mesons observed through their decay to $J/\psi K^{\pm}$, using the ATLAS detector at $\sqrt{s} = 8\,\mathrm{TeV}$

Master's Thesis

KIRCHHOFF-INSTITUT FÜR PHYSIK

Department of Physics and Astronomy

University of Heidelberg

Master's thesis

in Physics

submitted by

Simon Schröder

born in Bielefeld

2014

A measurement of the production cross section of $B_c^{\pm}$ mesons observed through their decay to $J/\psi\pi^{\pm}$, relative to the production cross section of $B^{\pm}$ mesons observed through their decay to $J/\psi K^{\pm}$, using the ATLAS detector at $\sqrt{s} = 8\,\mathrm{TeV}$

This master's thesis has been carried out by Simon Schröder

at the

Kirchhoff-Institute for Physics

under the supervision of

Prof. Dr. Hans-Christian Schultz-Coulon,

Prof. Dr. Sally Seidel

Eine Messung des Produktionswirkungsquerschnitts von $B_c^\pm$ Mesonen, die durch den Zerfall zu $J/\psi\pi^\pm$ beobachtet werden, relativ zu dem Produktionswirkungsquerschnitt von $B^\pm$ Mesonen, die durch den Zerfall zu $J/\psi K^\pm$ beobachtet werden, mit dem ATLAS Detektor bei $\sqrt{s} = 8\,\text{TeV}$:

Vorliegende Arbeit ist ein Beitrag zur Messung des relativen totalen und differentiellen Wirkungsquerschnitts multipliziert mit dem Zweigverhältnis (BR) für die Produktion von $B_c^\pm$ mit dem ATLAS Detektor am LHC bei einer Schwerpunktsenergie von $\sqrt{s} = 8\,\text{TeV}$. Der Produktions-Wirkungsquerschnitt für $B^\pm$ wird als Referenz benutzt. Die hadronischen Zerfallskanäle $B_c^\pm \to J/\psi\pi^\pm$ und $B^\pm \to J/\psi K^\pm$ bieten vollständig rekonstruierbare Zerfälle, die für diese Messung genutzt werden. Die Untersuchung erfolgt mit $p_\text{T}(B_c^\pm) > 13\,\text{GeV}$ im Barrel-Bereich des inneren Detektors, der den Bereich $|\eta| < 1.05$ der Pseudorapidität abdeckt. Die Daten werden in zwei Bereiche in p_T untergliedert. Die Anzahl der Zerfälle wird aus dem Fit an die Verteilung der invarianten Masse für sowohl $B_c^\pm$ als auch $B^\pm$ bestimmt und auf die Auswahleffizienz korrigiert. Letztendlich wird $\frac{\sigma(B_c^\pm)\times BR(B_c^\pm\to J/\psi\pi^\pm)}{\sigma(B^\pm)\times BR(B^\pm\to J/\psi K^\pm)}$ in den zwei Bereichen berechnet, die zugehörigen Messunsicherheiten untersucht und der relative Produktions-Wirkungsquerschnitt multipliziert mit dem Zweigverhältnis berichtet.

A measurement of the production cross section of $B_c^\pm$ mesons observed through their decay to $J/\psi\pi^\pm$, relative to the production cross section of $B^\pm$ mesons observed through their decay to $J/\psi K^\pm$, using the ATLAS detector at $\sqrt{s} = 8\,\text{TeV}$:

The thesis in hand is a contribution towards the measurement of the relative total and differential cross sections times branching ratio (BR) for the production of $B_c^\pm$ mesons with the ATLAS experiment at the LHC at a center of mass energy of $\sqrt{s} = 8\,\text{TeV}$. The production cross section for the $B^\pm$ meson is used as a reference. The hadronic decay channels $B_c^\pm \to J/\psi\pi^\pm$ and $B^\pm \to J/\psi K^\pm$ provide fully reconstructable events which are used for this measurement. The analysis is done for $p_\text{T}(B_c^\pm) > 13\,\text{GeV}$ in the barrel region of the inner detector covering the pseudorapidity range $|\eta| < 1.05$. The data are divided into two bins in p_T. The number of events is extracted from the fit to the invariant mass distributions for both the $B_c^\pm$ and the $B^\pm$ and corrected for the selection efficiency. Finally, $\frac{\sigma(B_c^\pm)\times BR(B_c^\pm\to J/\psi\pi^\pm)}{\sigma(B^\pm)\times BR(B^\pm\to J/\psi K^\pm)}$ is calculated for each bin, the uncertainties are evaluated, and the relative production cross section times branching ratio is reported.

Contents

1 Introduction

The *Standard Model of Particle Physics* gives a theoretical description of fundamental particles and the interactions between them. It is able to describe many measurements in particle physics with high precision. After the recent discovery of the Higgs boson[1; 2], the Standard Model is even more firmly established. The corresponding Higgs mechanism can be used to explain the origin of the fermion masses and the masses of the W and Z bosons. It is important evidence in support of the model. However, there are still open questions which can not be explained by that model. Probably the most important are the questions of the origin of dark matter and dark energy, the asymmetry between matter and antimatter in our universe, and the difference in magnitudes between the gravitational force and the other fundamental forces. This is linked to the idea of possible extra dimensions or new symmetries.

The *Large Hadron Collider* (LHC)[3] at the Swiss-French border in Geneva is designed to address these unanswered questions and to further investigate the interactions described by the Standard Model. It is the world's biggest particle accelerator and collides protons with a center of mass energy of $\sqrt{s} = 8\,\text{TeV}$ (in 2012) at four different interaction points. At these points are the ATLAS[1], CMS[2], ALICE[3], and LHCb[4] detectors. Whereas LHCb is able to perform high efficiency measurements in the longitudinal direction, ATLAS and CMS have high transverse resolution. ALICE concentrates on the investigation of the *quark-gluon plasma*, a state where quarks and gluons are deconfined.

This study uses data from the ATLAS detector to measure the cross section times branching ratio (BR) for the production of the $B_c^\pm$ meson relative to those of the $B^\pm$ meson. The measurement has high efficiency in the transverse region. The $B_c^\pm$ meson is the only system with two different heavy flavors, beauty and charm. It was first observed by Tevatron[4]. In 2012 it was observed at the

[1]abbrevation: **A** **T**oroidal **L**HC **A**pparatu**S**
[2]abbrevation: **C**ompact **M**uon **S**olenoid
[3]abbrevation: **A** **L**arge **I**on **C**ollider **E**xperiment
[4]abbrevation: **L**arge **H**adron **C**ollider **b**eauty

ATLAS detector[5]. At the LHC it is predominantly produced by gluon-gluon fusion. This measurement can be used as input for perturbative QCD and lattice models in order to improve understanding of the mechanisms for production and hadronization of heavy quarks.

In Section 2 the Standard Model is introduced in a phenomenological manner. The ATLAS experiment is described in Section 3. Before the selection of the B_c^+ events is explained (Section 5), an overview of previous related measurements and cross section predictions for the B_c^+ is given (Section 4). Finally the selection criteria are applied in the measurement of the relative production cross section times branching ratio and the result is corrected for the efficiency of the reconstruction (Section 6). The results are summarized in the Conclusion (Section 7) and an overview of possibilities for further investigation is given (Section 8).

2 Standard Model of Particle Physics

The Standard Model of Particle Physics is a quantum field theory encompassing *Quantum-Electro-Dynamics* (QED), *Quantum-Chromo-Dynamics* (QCD), and the theory of the weak interaction. QED gives a description of the interaction due to the electric charge of particles, whereas QCD describes the strong interaction due to their color charge (see 2.1). Particle properties are derived from the quantum fields.

2.1 Particles of the Standard Model

Particles can be classified by their spin as *fermions* and *bosons*. A fermion has a spin of $(2n + 1)/2$ with n being any integer. The bosons are characterized by a spin of n. According to the Pauli Principle, fermions have to differ in at least one of their characteristics, whereas several bosons can occupy the same quantum state. The bosons mediate the interactions between the fermions. The fermions include *leptons* such as the electron and the neutrinos, and *quarks*. The quarks can not be observed individually, because they are subject to the *strong force*. They combine to form particles called *hadrons*. The fermions and their properties are listed in Table 2.1. For each of them there exists an anti-particle with the same characteristics, but opposite charge.

Fermion	Generation I	II	III	Charge /e	Interactions
Quarks	u	c	t	+2/3	el.-magn., weak, strong
	d	s	b	-1/3	
Leptons	e	μ	τ	-1	el.-magn., weak
	ν_e	ν_μ	ν_τ	0	weak

Table 2.1: Elementary fermions of the Standard Model of Particle Physics, and their charge and interaction properties. Only the quarks carry color charge and are thus subject to the strong interaction mediated by gluons. Quarks and leptons carry a spin of 1/2.

There are six quark flavors, which are grouped in three generations according to their masses. The up (u) and down (d) quarks are the lightest quarks, the top (t) and bottom (b) the heaviest. The masses of the charm (c) and strange (s) lie in between. Quarks interact via all three fundamental interactions of the Standard Model. They carry either an electric charge of $e \cdot 2/3$ or $-e \cdot 1/3$. Thus, they are subject to the electromagnetic interaction which couples to electric charge. The quarks carry *color charge* as well. There are three different colors, allowing the strong interaction to bind quarks together. A hadron has to be color-neutral and have an electric charge of $\pm n \cdot e$, $n \in \mathbb{Z}$. This can be achieved by combining three quarks of different colors into one particle, a *baryon*. Another way of obtaining color-neutral particles is combining color and anti-color. Since anti-quarks carry anti-color, a quark and an anti-quark can combine into a *meson*. Quarks also interact weakly. The weak interaction can convert a quark into one with different flavor. The probability for such a flavor change is characterized by the *Cabibbo-Kobayashi-Maskawa* (CKM) matrix. Changes within one quark-generation are most probable. Changes between different generations are *Cabibbo-suppressed*.

Additionally, there exist six leptons. These are: electron (e), muon (μ), tau (τ) and their corresponding neutrinos (ν_e, ν_μ, ν_τ). All of them can interact via the weak interaction, but only the e, μ, and τ have an electric charge and are consequently able to interact electromagnetically as well.

Boson	Spin	Interaction	approx. range	Charge /e
W^+	1	weak	10^{-2} fm	1
W^-				-1
Z^0				0
γ		el.-magn.	∞	
g		strong	1 fm	
H	0	mass-coupling	-	

Table 2.2: Bosons of the Standard Model of Particle Physics, their properties and the interactions they carry.

The interactions are mediated by exchange of bosons (see Table 2.2). The gluon (g) is responsible for the strong interaction. There exist eight different gluons. The massless gluons have color themselves and can couple to one an-

other. This leads to the very short range of the strong interaction. The range of the weak interaction is even smaller. This is due to the mass of the exchange bosons ($W^{\pm}$, Z^0). Within the weak interactions there are *charged-current interactions* and *neutral-current interactions*. The charged-current interaction is carried by the $W^{\pm}$ bosons. A particle flavor is changed by the absorption or emission of a $W^{\pm}$. For example a μ^- will be transformed into a neutral ν_μ under absorption of a W^+. The neutral-current interaction, on the other hand, does not carry any electric charge. In a neutral current interaction a Z^0 boson is absorbed or emitted. It decays into a fermion/anti-fermion pair. The boson of the electromagnetic interaction is the photon γ. It couples to electric charge. The Higgs boson does not mediate the fundamental interactions, but gives the elementary particles their masses.

2.2 Cross section

If a bunch of particles of type α is made to pass head-on through a bunch of particles of type β and their overlap area is A, and the numbers of particles swept into that overlap area are N_α and N_β (at LHC $N_\alpha, N_\beta \leq 1.1 \cdot 10^{11}$ [3]) respectively, then the reaction rate $\dot{N}_{\text{react}}$ (number of reactions per unit time) is given by

$$\dot{N}_{\text{react}} = \sigma \cdot \frac{N_\alpha N_\beta f\, n}{A}, \tag{2.1}$$

where n is the number of bunches and f is the bunch crossing frequency. The σ is called the *cross section*. It is a measure of the probability of a certain reaction and has the dimension of an area. When the particle has more than one mode for decay the number of events measured, N_{meas}, is given by the product of N_{react} and the *branching ratio*. Hence, the branching ratio is the ratio of the number of particles undergoing a certain process to the total number of particles.

Using the definition of the *luminosity*,

$$L = \frac{n\, N_\alpha\, N_\beta\, f}{A}, \tag{2.2}$$

(2.1) can be rewritten as

$$\dot{N}_{\text{react}} = L\, \sigma. \tag{2.3}$$

The luminosity delivered to the experiments decreases during each run, because

of the decrease in N_α and N_β with each interaction. Integration over time of (2.2) gives the *integrated luminosity*

$$L^{\text{int}} = \int L \, \mathrm{d}t. \tag{2.4}$$

This can be used to replace the reaction rate $\dot{N}_{\text{react}}$ by the number of outgoing particles $N = \int \dot{N}_{\text{react}} \, \mathrm{d}t$ and express the production cross section as the ratio of the number of final state particles to the integrated luminosity

$$\sigma = \frac{N}{L^{\text{int}}}. \tag{2.5}$$

Theoretical cross section predictions in QED make use of *Fermi's Golden Rule*, which gives the transition rate $\dot{N}_{\text{react}}$ as a function of the transition matrix element $M_{f,i}$ between the initial quantum state $|i\rangle$ and the final state $|f\rangle$ and the phase space $\rho(E_f)$ of the final state:

$$\dot{N}_{\text{react}} = 2\pi |M_{f,i}|^2 \rho(E_f). \tag{2.6}$$

$M_{f,i}$ is given by $\langle f \,|\, H_{int} \,|\, i \rangle$ for the interaction Hamiltonian H_{int}. The cross section $\sigma = \dot{N}_{\text{react}}/L$ is the ratio of the transition rate to the luminosity L. In Fermi's Golden Rule an approximative calculation of the transition matrix elements is used.

The $B_c^\pm$ is a system made up of a b and a $\bar{c}$ (B_c^-) or $\bar{b}$ and c (B_c^+). Its cross section is calculated from two kinds of diagrams contributing to the matrix elements, *fragmentation diagrams* and *recombination diagrams*. The diagrams of recombination type represent the amplitude for the binding of $c(\bar{c})$ and $\bar{b}(b)$ quarks from independent pair production in hard parton scattering to form $B_c^+(B_c^-)$ mesons. This process is most important for small momenta[6].

The total cross section for inelastic scattering of the partons i and j carrying the proton momentum fractions x_1, x_2 is given by:

$$\sigma_{b\bar{b}} = \sum_{i,j} \int \mathrm{d}x_1 \mathrm{d}x_2 f_i f_j \hat{\sigma}_{i,j}, \tag{2.7}$$

where f_i, f_j are the parton distributions for each parton inside the respective colliding protons. The short distance inelastic scattering cross section $\hat{\sigma}_{b\bar{b}}$ can be calculated in a perturbative manner for high energies (expansion in the strong

coupling α_S). At leading order, the calculation is exactly as for a QED process. At higher orders an exact calculation is not possible. Approximations make use of the factorization theorem[7], which allows the non-perturbative part of (2.7) to be factored out and calculated independently.

In this analysis only momenta higher than the $B_c^{\pm}$ mass play a role and the most important processes in the $B_c^{\pm}$ cross section are the contributions of the fragmentation type diagrams[8]. The differential production cross section for a specific b-hadron can be well estimated by the convolution of the b quark production cross section in inelastic collisions $\sigma_{b\bar{b}}$ (2.7) and the fragmentation function times the fragmentation fraction[9]. The fragmentation function is a single particle distribution[10]. It describes the formation of hadrons from the quark-antiquark pair. Its integral over the fraction of the parton's energy equals one, so that all produced b quarks form hadrons. The fragmentation fraction is the fraction of the contribution of the specific hadron to the fragmentation product. The measurement of differential cross sections provides information about the fragmentation fractions.

In this production process, first, a quark-antiquark pair is produced in hard scattering[11]. Secondly, they may radiate secondary gluons by the strong interaction. When the quarks separate, the potential energy due to the color interaction between the two quarks grows until it has increased so much that another quark-antiquark pair is created from the vacuum. This process repeats several times and the system creates clusters of quarks and gluons with zero net color and low internal momentum. The color coupling turns them into hadrons. The fragmentation of $b\bar{b}$ creating a $c\bar{c}$ pair is by far the dominant contribution over the fragmentation of $c\bar{c}$ creating a $b\bar{b}$ pair[8].

2.3 B-physics

This section focuses on the physics of hadrons containing a b quark relevant for this study. The b quark was proposed in 1973[12] together with the introduction of the CKM matrix. The CKM matrix describes the probability of transition between different quark flavors (weak interaction). Since the b is the lighter element of the third quark generation, its decay requires generation change. Therefore, the study of B systems can be used to constrain the Standard Model Charge-Parity violation mechanism described by the CKM matrix[13].

With its two heavy flavors the $B_c^{\pm}$ is a unique system for the study of heavy quark dynamics, different from the model of $q\bar{q}$ mesons (quarkonia), which can annihilate. In its production two heavy quark-antiquark pairs must be created, which explains the low value of the $B_c^{\pm}$ production cross section. Whereas the $b\bar{b}$ production is of the order of α_s^2, with α_s being the strong coupling, the leading QCD order for the creation of bc systems is α_s^4. It begins with the creation of a $\bar{b}(b)$ and $c(\bar{c})$ quark by parton collision, which then bind to form the $B_c^+(B_c^-)$ meson. Some excited states of the $B_c^{\pm}$ will cascade down to the ground state. Hence, the measured production cross section is the sum of the production cross sections for the ground state and through cascades from excited states. Only at high energy and luminosity (see (2.2)) can sufficient $B_c^{\pm}$ events be collected for a cross section measurement. The hadronic production of the $B_c^{\pm}$ is dominated by the parton subprocess of gluon-gluon fusion $gg \to B_c^+ + b + \bar{c}(B_c^- + \bar{b} + c)$[14]. The heavy-quark content allows a non-relativistic treatment of the quark motion, and the sea quark contribution is negligible.

The $B_c^{\pm}$ meson has a mean lifetime of (0.45 ± 0.04) ps[15]. It can only be measured through it decay products, because only very few will reach the active parts of the detector. There are three different ways for the $B_c^{\pm}$ to decay. There could be a decay of the $\bar{b}(b$ for the $B_c^-)$ with a spectator $c(\bar{c})$ or the other way around. Additionally there is an annihilation channel. In the annihilation process the $B_c^{\pm}$ decays into quarks or leptons. Two decays are especially suitable for experimental measurement. The semileptonic channel $B_{\pm}^+ \to J/\psi\mu\nu_\mu$ was used in the observation by the CDF collaboration[4]. The J/ψ is a meson with the quark content $c\bar{c}$. The second possibility has a smaller branching ratio, which means that it occurs less frequently. However, it allows for a better mass measurement because it does not involve a ν whose energy can only be inferred by ATLAS from missing energy. This is the $B_c^{\pm} \to J/\psi\pi^{\pm}$ decay involving the pion $\pi^{\pm}$, a meson which is made up of $u\bar{d}$ ($\bar{u}d$ for the π^-) quarks. This channel is used in this analysis. The evidence for this decay was given by the CDF Collaboration in 2006[16]. It was used in the B_c observations by ATLAS[5] and LHCb[17]. The branching ratio is $0.13\% \pm 0.08\%$[13].

An identical decay topology can be used to measure the $B^{\pm}$ meson. The $B^{\pm}$ is composed of $\bar{b}$ and u for the B^+, and b and $\bar{u}$ for the B^-. It decays in about (1.64 ± 0.01) ps[18]. Hence, it can only be measured through its decay products as well. The decay channel used in this measurement is the decay into a J/ψ and a

kaon (K^+): $B^+ \to J/\psi K^+$. The K^+ is a meson composed of $u\,\bar{s}$. The branching ratio for this channel is $BR(B^\pm \to J/\psi K^\pm) \cdot BR(J/\psi \to \mu^+\mu^-) = 6.01 \cdot 10^{-3}\,\%$ [13]. The branching ratio $BR(B^\pm \to J/\psi K^\pm) \approx 0.101\,\%$ is thus comparable to the one for the $B_c^\pm \to J/\psi\pi^\pm$ decay. $B^\pm$ events are produced much more frequently, because only one heavy quark-antiquark pair needs to be created. Consequently, many more $B^\pm$ than $B_c^\pm$ can be observed with the signature of a decay into J/ψ and hadron.

The $B^\pm$ meson is used as the reference in the relative production cross section times BR measurement. Because of its similar decay topology, some systematics will cancel. Note that the results are reported for the B^+ and the B_c^+ meson, but are derived from both charged states using the $B^\pm \to J/\psi K^\pm$ and the $B_c^\pm \to J/\psi\pi^\pm$ decays. The charge conjugate production cross section is assumed to be identical. This assumption is implemented directly in the Monte Carlo generators and was confirmed for the $B^\pm \to J/\psi K^\pm$ decay[9].

The measurement of B particles in a hadron collider requires high particle fluxes with long beam lifetime, magnetic spectrometers with broad acceptance providing good momentum and mass resolution, radiation hard vertex detectors, excellent particle identification, and efficient triggering and high speed data acquisition[19]. The LHC provides high particle flux and has in the LHCb an experiment dedicated to B-physics. While this detector examines particles in the forward direction ($\eta > 2.5$), the general purpose detectors ATLAS and CMS have the capability to perform B-physics measurements in the transverse region ($|\eta| < 2.5$).

3 The Experiment

3.1 LHC

The Large Hadron Collider (LHC)[3] at CERN[1] is designed to search for the Higgs boson, look for physics beyond the Standard Model, solve further puzzles like the matter-antimatter asymmetry, and perform precision measurements of Standard Model processes[13]. It consists of two superconducting accelerator rings[3]. The larger ring has a circumference of 27 km. Because of its size, its radiative energy loss due to the acceleration of charged particles, the *bremsstrahlung*, is kept low.

Protons are accelerated in opposite directions within two separate vacuum chambers. The two beams can be brought into collision at the four interaction regions where the detectors are located. Here they share a common beam pipe. The acceleration happens in a sequence. Protons are produced in a hydrogen source, when the electrons are stripped off by an electric field. Then the protons are accelerated within the linear accelerator *Linac2* to an energy of 50 MeV. The next acceleration stage, the *Proton Synchrotron Booster* (PSB), accelerates the protons to 1.4 GeV. They are further accelerated in the *Proton Synchrotron* (PS) (25 GeV) and the *Super Proton Synchrotron* (SPS) where they finally reach 450 GeV. They are then passed into the big accelerator ring of the LHC. In the LHC it takes 20 minutes for the protons to reach their final energy, but the beams circulate for many hours inside the beam pipes under operation conditions.

Since heavy ions are produced in a different source, they are accelerated in another linear accelerator (*Linac3*). Afterwards they are passed to the *Low Energy Ion Ring* and finally follow the same acceleration steps as the protons starting with the PS. These accelerator stages provide a beam with bunched structure. The gaps between the bunches are used for synchronization, calibration, and providing reset to the electronics.

[1] European Center for Nuclear Research (French: **C**onseil **E**uropéen pour la **R**echerche **N**ucléaire)

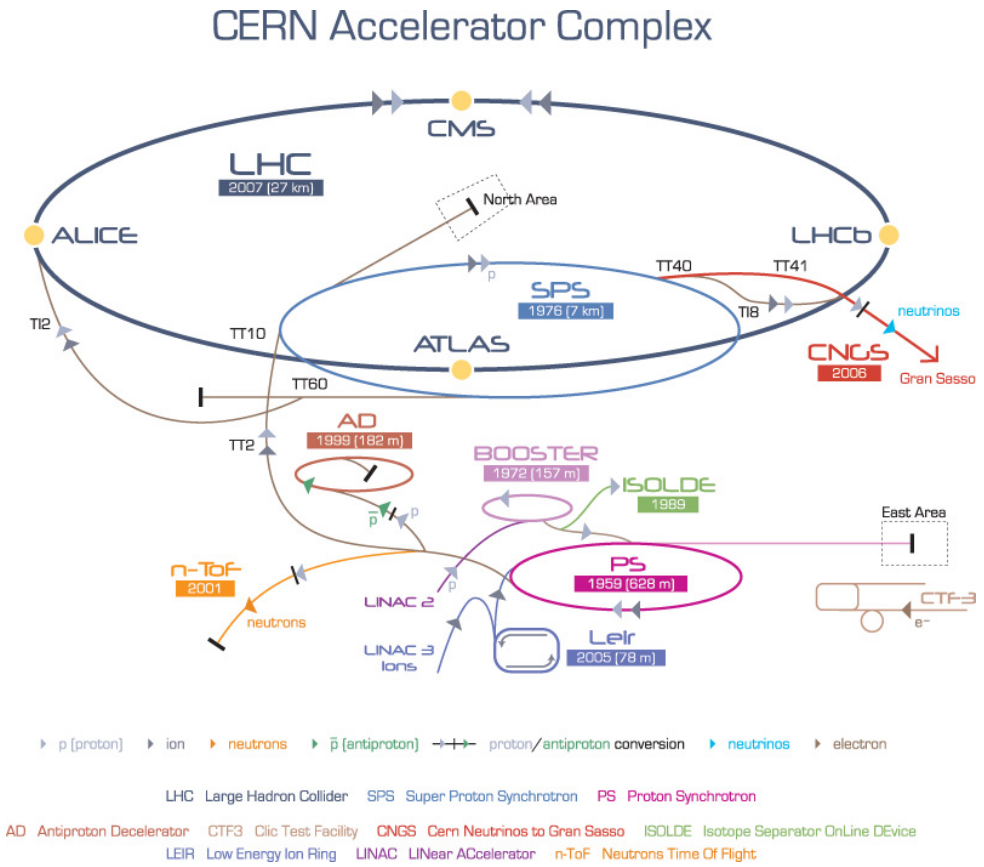

Figure 3.1: The different accelerator stages for protons and lead ions.

A collider such as this is characterized by its center of mass energy $\sqrt{s}$ and the luminosity L. The LHC is designed to reach a center of mass energy of $\sqrt{s} = 14\,\text{TeV}$ and a peak luminosity of $10^{34}\,\text{cm}^{-2}\text{s}^{-1}$ at the ATLAS and CMS experiments[3]. It operated with a center of mass energy of $\sqrt{s} = 7\,\text{TeV}$ in 2011, and this was increased to $\sqrt{s} = 8\,\text{TeV}$ in the beginning of 2012. Currently the accelerator is shut down to be upgraded in order to run with the design center of mass energy. This analysis uses data obtained by the ATLAS detector in 2012 with a center of mass energy of $\sqrt{s} = 8\,\text{TeV}$.

3.2 ATLAS

The ATLAS detector[20] is the largest detector at the LHC. It is a multipurpose detector designed to search for signals of new physics and measure Standard Model processes with the highest accuracy at the high energy frontier. Its layout is designed to characterize the known particles and look for missing energy as well. It is sensitive to objects that would be produced by new physics processes such as: electrons with high transverse momentum p_{T} (the projection of the momentum onto the plane perpendicular to the beam axis), photons, muons, τ's and jets[19] (streams of hadrons which are in close proximity to one another in their trajectory). These jets can contain B mesons.

3.2.1 Geometry

A schematic drawing of the detector is shown in Figure 3.2. It is 44 m long, 25 m high, and weighs roughly $7 \cdot 10^6$ kg[20]. The interaction point in the middle of the detector is used as the center of a right-handed coordinate system. The beam axis is the z axis, while the x-y plane is perpendicular to it. The positive x-axis points to the center of the LHC ring, and the y axis points upwards. The side of the detector towards positive z is called side A and the side towards negative z is the C-side. The angle ϕ (ranging from 0 to 2π) is measured around the z-axis. The polar angle θ (ranging from 0 to π) is measured from the z-axis. The *pseudorapidity*

$$\eta = -\ln\left(\tan\left(\frac{\theta}{2}\right)\right) \tag{3.1}$$

can be used alternatively. For sufficiently high velocities and low particle masses the pseudorapidity becomes the same as the *rapidity*

$$y = \frac{1}{2}\ln\left(\frac{E + p_{\mathrm{L}}}{E - p_{\mathrm{L}}}\right). \tag{3.2}$$

E is the particle's energy and p_{L} its longitudinal momentum (momentum component along the z-axis). The rapidity y is a generalization of the velocity $\beta_{\mathrm{L}} = p_{\mathrm{L}}/E$. The difference of rapidities is the same in every system moving with constant velocity, i.e., rapidity difference is *Lorentz invariant*. At LHC energies the rapidity and pseudorapidity can be assumed to be the same for protons. Hence, the pseudorapidity difference can be treated as Lorentz invariant.

3.2.2 Setup and components

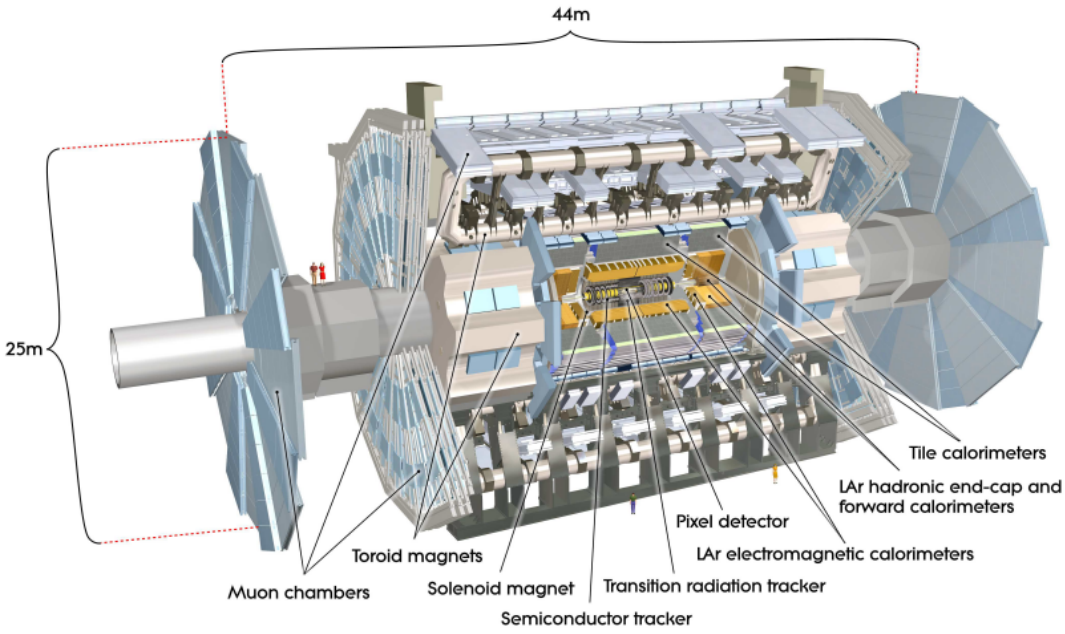

Figure 3.2: Schematic picture of the ATLAS detector. Humans are shown to illustrate the detector size.

ATLAS has several different layers. The *Inner Detector* (ID) is closest to the interaction point. It is used to identify and locate the vertices, recognize certain patterns, determine the particles' charge and momentum, and identify electrons. The measurement of energy is done by the *Electromagnetic Calorimeter* and the *Hadronic Calorimeter* surrounding the Inner Detector. The outer detector layer is the *Muon Spectrometer* (MS), which detects charged particles that exit the calorimeters and measures their momentum. The detector chambers are concentric around the beam axis in the barrel region and perpendicular to the beam in the end caps. The muonic *trigger* makes use of information from these detector chambers to filter events of interest before the offline data analysis takes place.

The signatures of different particle species in the subsystems of the ATLAS detector are indicated in Figure 3.3. ATLAS does not have particle identification to distinguish between different hadrons. (This results in the exclusive backgrounds, section 5.1.) The components most relevant to the B_c^+ reconstruction are the ID and the MS. In the $B_c^+ \to J/\psi\pi^+$ decay, the J/ψ meson

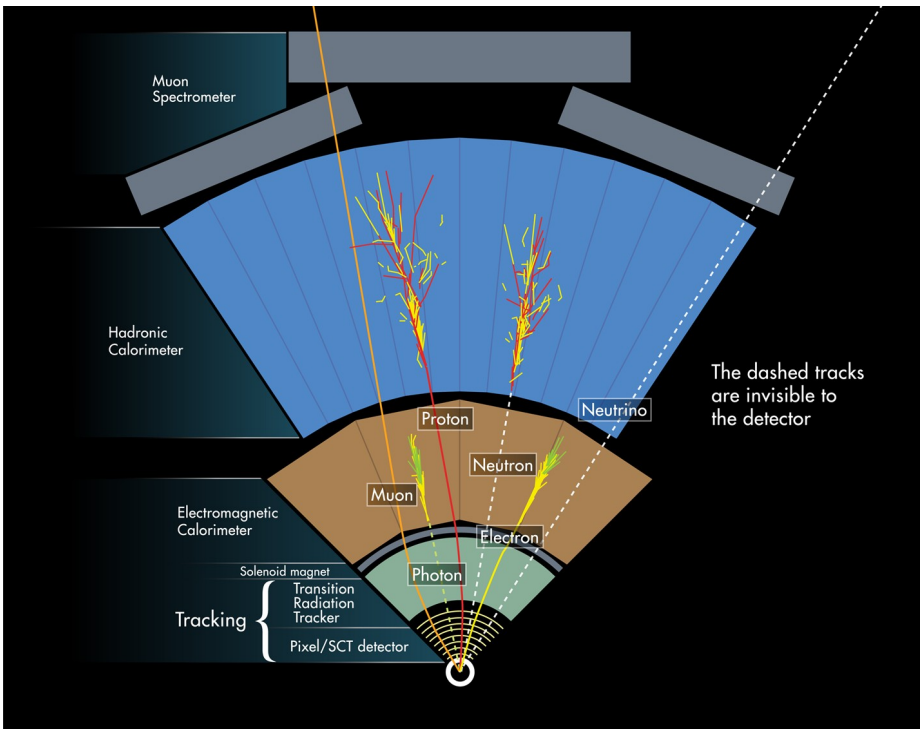

Figure 3.3: Particle signatures in ATLAS. The dashed lines are invisible to the detector.

is reconstructed from its decay into a muon anti-muon pair. These muons leave a signal in the ID, MS, and electromagnetic calorimeter. The energy of the π^+ could measured in the electromagnetic and hadronic calorimeters. The energy measurement of the calorimeters is not used in this analysis. The muons are identified by the MS and the ID is used for the identification of the vertices and the momentum measurements.

Inner Detector

The Inner Detector consists of the *Pixel detector*, *Silicon microstrip tracker* (SCT) and *Transition radiation tracker* (TRT)[20]. Its layout is depicted in Figure 3.4. The silicon pixel detectors are most important for the identification of hadronic tracks including b-jets[19]. The Pixel detector and SCT are precision tracking detectors for $|\eta| < 2.5$. The Pixel detector has high granularity around the vertex region, with a pixel size of $50 \times 400\,\mu\text{m}^2$ ($z \times R - \phi$). The pixel modules are installed in three layers. All in all there are 1744 pixel modules with 46080 readout channels on each of them.

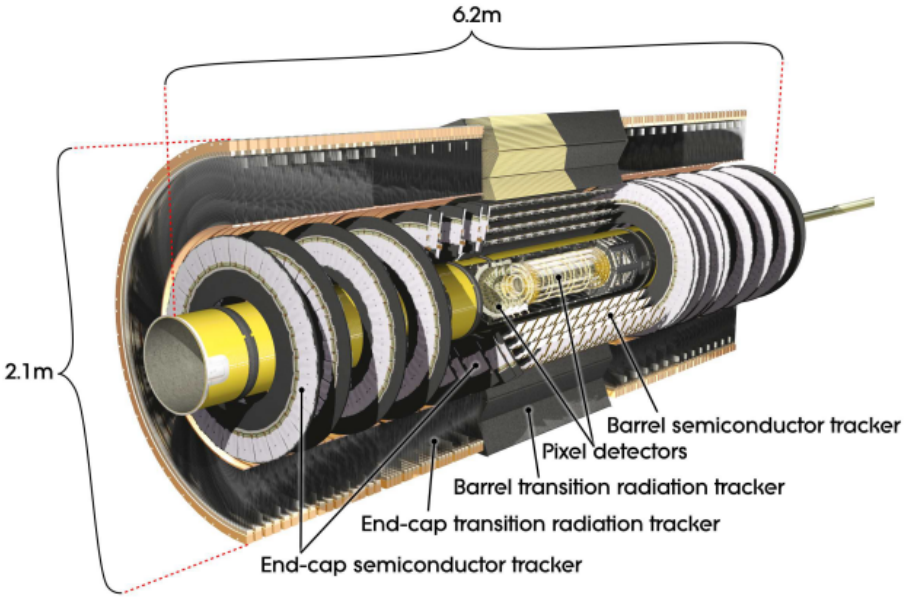

Figure 3.4: Cut-away view of the Inner Detector.

The Pixel detector is followed by the SCT. The SCT includes four coaxial layers in the barrel region and nine layers in the end caps. Each of these layers is a composition of two back-to-back silicon detectors. The readout strips of the pairs use small angle stereo. In total there are more than $6 \cdot 10^6$ readout channels in the SCT.

The TRT is the outer part of the ID. The TRT contains up to 73 layers of straws interleaved with fibers in the barrel region and 160 planes interleaved with polypropylene radiator foils in the end cap regions. They provide transition radiation for electron identification. Each straw has a diameter of 4 mm and is filled with a special gas mixture kept at slight overpressure. A voltage of $-1530\,\mathrm{V}$ between the gold-coated tungsten wire anode in the center of each straw and the cathode permits the measurement of electron trajectories with an accuracy of $130\,\mu\mathrm{m}$.

Transition radiation is electromagnetic radiation emitted by charged particles which pass through a dielectric boundary layer. The absorption of the photons in the gas leads to signals which can be distinguished from the signals of charged particles by their amplitude. These signals can be used to separate particles, for example electrons and pions.

The components of the ID are immersed in a 2 T magnetic field. This field is created by a superconducting *solenoid magnet*. Charged particles are deflected by the *Lorentz force*, which makes a measurement of their momentum possible. The particle has to have at least three hits in the ID, as otherwise the momentum can not be reconstructed. In this analysis more than eight hits in the Pixel and SCT detectors are required.

Calorimeters

The Calorimeters around the ID absorb the particles to measure their energies. The energy measurement of the *electromagnetic calorimeter* is through the electromagnetic interaction of particles. Hence, it is best for measuring the energy of photons and charged particles. The *radiation length* X_0 is a measure of the energy loss of high energy electromagnetically interacting particles in a material. It is defined as the mean distance over which an electron loses all but e^{-1} of its energy. At the same time it is 7/9 of the mean free path for pair production of photons. The thickness of the electromagnetic calorimeter is between $22\,X_0$ and $33\,X_0$ [20].

The electromagnetic calorimeter is followed by the hadronic calorimeter. The hadronic particles interact electromagnetically and through the strong force with the nuclei of the calorimeter material. The Tile calorimeter is the part of the hadronic calorimeter located directly behind the electromagnetic barrel calorimeter and covers a pseudorapidity interval of $|\eta| < 1.7$. It is 7.4 *interaction lengths* λ thick. The interaction length λ is defined such that only $1/e$ of the particles do not undergo an inelastic interaction within λ.

This analysis does not use information from the calorimeters. Nevertheless, the calorimeters take part in the detection by absorbing most particles and preventing them from reaching the Muon Spectrometer.

Muon Spectrometer

Whereas in this analysis the π^+ deposits all of its energy in the calorimeters, the J/ψ decays into a $\mu^+\mu^-$ pair and the calorimeters do not absorb most muons. The muons will reach the outermost part of the detector, the Muon Spectrometer (MS)[21]. The whole muon detection system is indicated in Figure 3.5.

In the barrel region ($|\eta| < 1.4$), muons are measured in three concentric layers around the beam axis (at $5\,\mathrm{m}, 7.5\,\mathrm{m}$, and $10\,\mathrm{m}$ distance from the beam)[20]

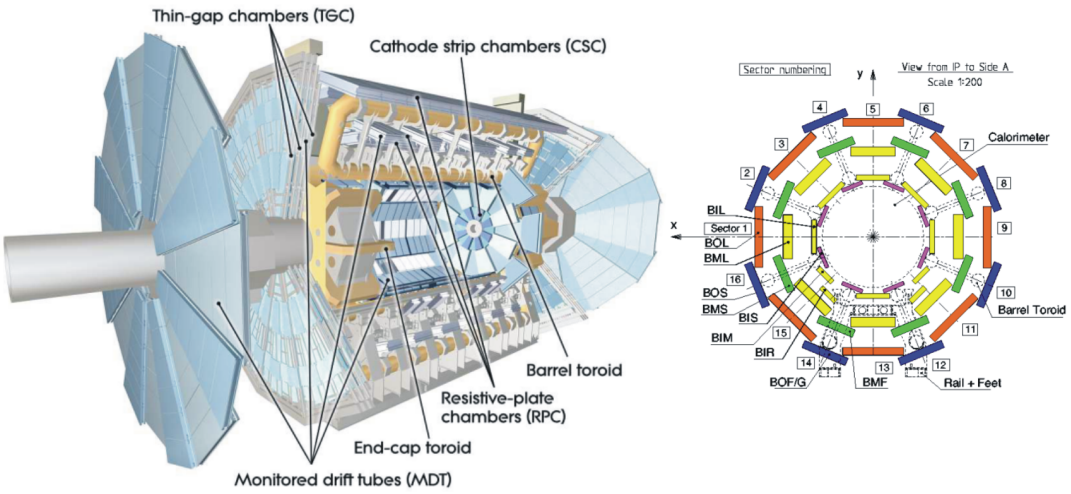

Figure 3.5: Schematic picture of the Muon detection system at ATLAS (left). The barrel Muon Spectrometer consists of three layers of eight small and eight large chambers (right).

using *Monitored Drift Tubes* (MDTs) and fast *Resistive Plate Chambers* (RPCs). There are three times eight modules placed in accordance with the symmetry of the toroid as shown in Figure 3.5[20]. Each module is subdivided into a large and a small sector leading to an overlap in ϕ. They achieve a resolution of $50\,\mu$m, which results in 10% resolution in p_{T} for $p_{\mathrm{T}} \approx 1\,\mathrm{TeV}$ tracks. The MS barrel has a gap at $\eta \approx 0$ which allows service to the solenoid magnet, the calorimeters, and the Inner Detector. This gap varies in size. It is $< 2\,\mathrm{m}$. The toroid provides a magnetic field of $0.5\,\mathrm{T}$ allowing the measurement of the momentum. The magnetic field of the end caps dominates in the end cap region of $|\eta| > 1.6$, while the barrel region $|\eta| < 1.4$ is dominated by the magnetic field of the barrel solenoid. The magnetic field in between, in the transition region, is a combination of both fields.

In the end caps three chambers are installed vertically[21]. Here *Thin Gap Chambers* (TGCs) are used for the *trigger* (see Section 3.2.3) and MDTs are responsible for the precision measurement of muon tracks. Only for the innermost ring of the end caps with $|\eta| > 2$ *Cathode Strip Chambers* (CSCs) are used. Here the high particle fluxes require more radiation tolerance. The CSCs are multiwire proportional chambers with cathode planes segmented in orthogonal strips. They are complemented by the MDTs in the four end cap wheels (at $7.4\,\mathrm{m}$, $10.8\,\mathrm{m}$, $14.0\,\mathrm{m}$, and $21.5\,\mathrm{m}$ distance from the interaction point). The

MDTs have a maximum counting rate of about 150 Hz/cm^2. The CSCs allow for higher counting rates. A measurement of the muon momentum in the pseudorapidity range $|\eta| < 2.7$, and triggering in $|\eta| < 2.4$, are possible. The MDTs consist of three to eight layers of drift tubes filled with an Ar-CO_2 gas mixture which is held at 3 bar. This gas mixture shows nonlinear behavior leading to a reduction of spatial resolution at high counting rates. A 50 μm diameter tungsten-rhenium wire is held at a potential of 3080 V and collects the electrons from the ionization of the gas. The end cap modules consist of eight small and eight big chambers as well.

Since a good muon measurement is important for the J/ψ particle (and finally the B_c^+) reconstruction in the measurement of the production cross section, only so-called combined muons[22] are used. A muon is "combined" when the track in the Inner Detector and the one in the MS can be matched after being reconstructed independently. Here, the momentum is measured in the ID and the MS is used to identify the muons. There are also muons which can be reconstructed only in the MS (Stand-alone muons), leave a track in the ID but only a track segment in the MS (Segment-tagged muons), or tracks in the ID which lead to an energy deposition in the calorimeter which is typical of minimum ionizing particles (calorimeter-tagged muons). Those types of muons are excluded from this analysis. Also, the measurement of the muon's momentum in the MS allows for a reduction of the data even before the offline analysis (triggering).

3.2.3 Trigger

At design luminosity there are approximately 10^6 proton-proton interactions each second [20], but the data recording rate is limited to about 200 Hz. Therefore, a majority of the events has to be rejected before recording, without unacceptable loss of signal. The rate of B production is 500 kHz[19]. Not all of the B events can be stored. Additionally, the B events compete with events satisfying the signatures for a wide variety of new physics processes. The trigger for B physics focuses on muons, which provide a high purity and good reconstruction efficiency. For $p_T > 6$ GeV nearly all muons come from B decays. Decisions are made at three trigger levels. The Level-1 (L1) trigger system uses information from the MS and the Calorimeter to decide if an event will be processed further or not. It reduces the data rate to approximately 75 kHz. The subsequent Level-2 (L2) trigger and Event Filter provide a further reduction to a final data-taking rate of about 200 Hz.

The L1 trigger searches for high transverse momentum muons, electrons, photons, jets, and τ-leptons decaying into hadrons as well as large missing and total transverse energy E_{T}. Transverse energy is defined by $E_{\mathrm{T}} = \sqrt{m^2 + p_{\mathrm{T}}^2}$. For this fast selection the MS is equipped with RPCs. There are three concentric layers of RPCs in the barrel. The first two layers are below and above the middle layer of MDTs. They are used for the low p_{T} trigger with $6\,\mathrm{GeV} < p_{\mathrm{T}} < 9\,\mathrm{GeV}$. The third layer is located above the outer MDT in the larger sectors and below it in the smaller sectors. It is necessary for the high p_{T} trigger with $9\,\mathrm{GeV} < p_{\mathrm{T}} < 35\,\mathrm{GeV}$. Each RPC includes ionization chambers made of two resistive plates at a voltage difference of 9.8 kV with the active gas in between. The signal is read out via capacitive coupling to metallic strips on the outer faces of the resistive plates. Aside from their importance for the trigger, the RPCs provide the second coordinate for the MDTs in the barrel region.

The TGCs are used in the forward region. They provide the second, azimuthal coordinate to complete the (radial) measurement of the MDTs and serve also for triggering the detector on muons. The middle MDT layer is complemented by seven TGC layers. They are structured in a triplet and two doublets. The triplet helps to reduce false coincidences from background hits, which are more likely in the forward region than in the barrel. The inner MDT layer is complemented by two TGC layers. They are multiwire proportional chambers with an active gas mixture of CO_2 and n-pentane. The applied voltage is about 2.9 kV on average.

The calorimeter trigger completes the L1 trigger. It uses a reduced granularity of the electromagnetic and hadronic calorimeters. It collects information about the transverse energy and the bunch crossing, identifies electron/photon and τ-lepton candidates, and characterizes their isolation. The transverse energy is measured by the preprocessor, which digitizes the input signals and associates them with the bunch crossings. The subsequent cluster processor looks for the electron/photon and τ-lepton candidates and examines whether their transverse energies lie above a certain (programmable) acceptance threshold. It can also verify whether certain isolation criteria are met. The jet/energy-sum processor identifies particle jets and produces global sums of scalar and missing transverse energy. The resulting counts and energy sums from the jet/energy-sum processor and the preprocessor are sent to the central trigger processor.

The central trigger processor (CTP) manages the trigger decisions. If there is a L1 Accept (L1A) decision, the data from the L1 calorimeter subsystems is forwarded to the data acquisition system. It also sends information about the trigger decision for all trigger items to the L2 trigger and the identified objects in units of η and ϕ to the region of interest (RoI) builder, which assembles it into a unique data fragment to be sent to the L2 supervisor. Furthermore, the CTP sets the luminosity blocks. A luminosity block is an interval containing just enough data after correction for dead time and prescale effects (random rejection of events, which pass the trigger, but are not recorded) such that the luminosity uncertainty is just limited by systematic effects. Such an interval is on the order of minutes.

For the L2 trigger, access to detailed information from all the ATLAS detector elements (including the Inner Detector) is necessary. Full granularity is used within the RoI, making up less than 3% of all data[23], as the basis for the L2 trigger decision. The triggering software makes the trigger decisions in several stages. Each stage requires additional data from more detectors. The algorithms identify features, such as tracks or calorimeter clusters, and determine whether these features meet the criteria (such as shower shape or transverse energy thresholds)[20]. For this analysis the two oppositely charged muons are required to originate from a common vertex with their invariant mass lying between 2.5 GeV and 4.3 GeV.

The last selection stage of the ATLAS trigger is the Event Filter (EF). It processes the events that are accepted by the L2 trigger. This is done with offline event reconstruction algorithms using full detector granularities. For this analysis a muon transverse momentum higher than 4 GeV for one of the muons and 6 GeV for the other one is required by the EF trigger for further event processing. It is also here that the events are channeled into the data streams: electrons, muons, jets, photons, $E_{\mathrm{T}}^{\mathrm{miss}}$, τ leptons, and B-physics. The events are recorded in files according to these streams. In this analysis the B-physics stream was used for the measurement and the optimization of the selection.

4 Predictions and Previous Measurements

The first searches for the B_c^+ meson at the LEP collider yielded a few candidate events and limits on some of its properties[14]. Experimental study of the B_c^+ and its properties started with its discovery by the CDF collaboration at Fermilab[4]. They observed the B_c^+ in 1998 in the semileptonic decay mode through proton antiproton collisions at $\sqrt{s} = 1.8\,\text{TeV}$. A total of $20.4^{+6.2}_{-5.5}$ B_c^+ events were observed. The mass was determined to be $(6.4 \pm 0.39_{\text{stat}} \pm 0.13_{\text{syst}})\,\text{GeV}$, and a lifetime of $(0.46^{+0.18}_{-0.16_{\text{stat}}} \pm 0.03_{\text{syst}})\,\text{ps}$ was measured. The observation in the hadronic decay mode allows for a more precise measurement of the B_c^+ mass. The first complete reconstruction in the hadronic mode was made by the CDF collaboration in 2006[24]. They observed 14.6 ± 4.6 events and increased the precision of the mass measurement to $(6285.7 \pm 5.3_{\text{stat}} \pm 1.2_{\text{syst}})\,\text{MeV}$. The B_c^+ has also been studied by the LHCb[17; 25], CMS[13; 26; 27] and ATLAS[5; 28] experiments at the LHC.

This thesis is a contribution towards the measurement of the differential relative and absolute production cross sections of the B_c^+ times branching ratio to $J/\psi\pi^+$ in pp collisions at the Large Hadron Collider with $\sqrt{s} = 8\,\text{TeV}$ by the ATLAS experiment. The cross section is differential in transverse momentum p_{T} of the B_c^+. Relative cross section measurements have been performed at $\sqrt{s} = 7\,\text{TeV}$ by LHCb[17] and CMS[27]. LHCb reported a relative cross section times branching fraction

$$\Big(\Big[\sigma_{B_c^+} \cdot \text{BR}(B_c^+ \to J/\psi\pi^+)\Big] \Big/ \Big[\sigma_{B^+} \cdot \text{BR}(B^+ \to J/\psi K^+)\Big]\Big)$$

of $(0.68 \pm 0.10_{\text{stat}} \pm 0.03_{\text{syst}} \pm 0.05_{\text{lifetime}})\,\%$ for $p_{\text{T}}(B_c^+) > 4\,\text{GeV}$ in the pseudorapidity range $2.5 < |\eta| < 4.5$. The third uncertainty is due to the calculation of the reconstruction efficiencies. It is dominated by the uncertainty on the B_c^+ lifetime. No cut (selection requirement) on the lifetime is used in the present analysis. CMS measured the relative cross section times branching ratio in the rapidity region $|y| < 1.6$ to be $(0.48 \pm 0.05_{\text{stat}} \pm 0.04_{\text{syst}}{}^{+0.05}_{-0.03\text{lifetime}})\,\%$. This

illustrates that a dependence of the production cross section on pseudorapidity is expected. A measurement of the (relative) B_c^+ production cross section times branching ratio,

$$\left[\sigma_{B_c^+} \cdot \mathrm{BR}(B_c^+ \to J/\psi\pi^+)\right] \Big/ \left[\sigma_{B^+} \cdot \mathrm{BR}(B^+ \to J/\psi K^+)\right] ,$$

with $\sqrt{s} = 8\,\mathrm{TeV}$ and binning in p_T has not been reported so far.

Theoretical predictions for the hadronic B_c^+ production cross section are reported by several authors[6; 8; 29; 30; 31; 32; 33]. In lowest order perturbation theory an uncertainty of a factor of 3 on the choice of the parametrization and the gluon distributions was observed by [29]. The results for the ground state are summarized in Table 4.1 for $\sqrt{s} = 1.8\,\mathrm{TeV}$, $\sqrt{s} = 14\,\mathrm{TeV}$, and $\sqrt{s} = 16\,\mathrm{TeV}$. A prediction for the production cross section at 8 TeV has not been given. Lowest order QCD perturbative theory for the hard scattering and non-relativistic potential models for the hadronization process are used by [30]. In [29] a standard calculation technique involving the approximation of negligible binding energy and relative momentum in the bound state is used and the quarks are assumed to be on shell with parallel momenta. The cross sections are computed at lowest order, including 36 matrix elements. The results of [30] agree with the calculations of [6; 29]. The choice of parametrization in [6; 29] is the same. Correction [32] to [6] improved the agreement between this model and the other predictions.

$\sigma(B_c^\pm)$ as calculated in:	$\sqrt{s} = 1.8\,\mathrm{TeV}$	$\sqrt{s} = 14\,\mathrm{TeV}$	$\sqrt{s} = 16\,\mathrm{TeV}$
[29]	3.2 nb to 6.4 nb	44 nb to 121 nb	78 nb to 140 nb
[30]		190 nb	
[8]	1 nb		12.3 nb
[6] with correction [32]	3.1 nb		50.3 nb
[31]	18.3 nb to 31.5 nb		
[33], $\lvert y\rvert < 1.5$	1.95 nb		

Table 4.1: The predictions for the total hadronic production cross section for the B_c^+ (here the charge conjugate is not implied) ground state at center of mass energies $\sqrt{s} = 1.8\,\mathrm{TeV}$, $\sqrt{s} = 14\,\mathrm{TeV}$, and $\sqrt{s} = 16\,\mathrm{TeV}$. The ranges given for [29; 31] reflect the dependence of the predictions on the choice of gluon distribution function and their scaling Q^2. All numbers are rescaled to $f_{B_c} = 500\,\mathrm{MeV}$.

These calculations depend on the measurement of the decay constant $f_{B_c^+}$ which in the non-relativistic approach is proportional to the absolute value of the wave function at the origin. This value lies between 160 MeV and 600 MeV[29] depending on the model and is a significant source of uncertainty on these predictions ($\sigma_{\text{theo}} \propto f_{B_c^+}^2$).

In this measurement not only will the ground state B_c^+ contribute, but also excited states which cascade down to the ground state. The ratio of the production cross section for excited states relative to that for the ground state is calculated in [6]. The excited B_c^+ mesons are produced about 1.3 to 2.5 times more frequently than the ground state B_c^+. In their calculation[6] fourth order (α_s^4) QCD perturbation theory was used with a fixed value for the strong coupling, $\alpha_s = 0.2$. Replacing α_s, with $\alpha_s(\hat{s})$, where $\hat{s}$ is the invariant mass squared of the interacting partons, would lead to a sevenfold decrease in the calculated cross sections[6].

In [8] two approaches are used together with perturbative QCD calculations at lowest order. Approach I considers only the production of quarks and their subsequent fragmentation into B_c^+. Approach II includes also the recombinatorial production. Only the results of Approach II are shown in Table 4.1, where the different predictions are presented. All calculations report that the differential cross section decreases for increasing transverse momentum $p_{\text{T}}(B_c^+)$.

The B^+ has a much higher production rate than the B_c^+. A measurement of its differential cross section times branching ratio for several bins in p_{T} and rapidity $|y|$ has been done by ATLAS[34] for $\sqrt{s} = 7\,\text{TeV}$. A similar measurement at $\sqrt{s} = 8\,\text{TeV}$ with ATLAS could be used to calculate the B_c^+ production cross section times branching ratio $\sigma(B_c^+)\text{BR}(B_c^+ \to J/\psi\pi^+) \cdot \text{BR}(J/\psi \to \mu^-\mu^+)$ from the measured relative cross section times branching ratios. The $\mu^+\mu^-$ branching ratio is $\text{BR}(J/\psi \to \mu^+\mu^-) = (5.93 \pm 0.06)\,\%$[35]. The spectra in p_{T} can be used in theoretical models to shed light on the mechanisms for production and hadronization of heavy quarks.

5 Selection of the Events

When measuring the cross sections times branching ratios,

$$\frac{\sigma(B_c^+) \cdot \mathrm{BR}(B_c^+ \to J/\psi\pi^+)}{\sigma(B^+) \cdot \mathrm{BR}(B^+ \to J/\psi K^+)},$$

a high yield in the number of events is required to keep statistical errors low. Since B_c^+ production is much less likely than B^+ production, the yield of B_c^+ events is crucial, so a study to optimize the selection criteria for the B_c^+ is undertaken (Section 5.2.1).

A first study of the B_c^+ selection was done at the time of the B_c^+ observation in the 2011 ATLAS data with a center of mass energy of $\sqrt{s} = 7\,\mathrm{GeV}$[5]. Applying these selection criteria to 2012 data leads to a reconstruction of $234 \pm 26_{\mathrm{stat}}$ B_c^+ and $33629 \pm 239_{\mathrm{stat}}$ B^+. In 2011 data, $82 \pm 17_{\mathrm{stat}}$ $B_c^+ \to J/\psi\pi^+$ decays were observed by ATLAS with the original event selection[5]. It is expected that a higher number of B_c^+ can be achieved, because the cuts might be relaxed and the integrated luminosity is about four times higher ($19.2\,\mathrm{fb}^{-1}$ in 2012 compared to $4.3\,\mathrm{fb}^{-1}$ in 2011). In this thesis it will be shown how far these cuts can be released.

More than 200 B_c^+ events are needed in $|\eta| < 1.05$ to measure the differential relative cross sections in two different bins in transverse momentum p_{T} within the barrel region of the inner detector. Each of these bins should contain more than 100 decays to have statistical uncertainties comparable with those in the B_c^+ observation. Some systematic errors will cancel by measuring the production rate for B_c^+ relative to B^+, because the mesons are observed through decays of identical decay topologies and the integrated luminosity is identical.

5.1 Composition of the background

It is important to minimize the uncertainty on the number of reconstructed B_c^+ decays, because it contributes directly to the precision of the cross section measurement. An understanding of the fake signal due to various background processes is necessary. The background comes from other decay processes which are interpreted as a $J/\psi\pi^+$ coming from a B_c^+ decay although there was no decay of the B_c^+, or particles other than the pion have been involved.

The $J/\psi \to \mu^+\mu^-$ decay gives a very distinct signature. Hence, the background is composed of combinations of J/ψ with hadron tracks falsely interpreted as $B_c^+ \to J/\psi\pi^+$ decays, because ATLAS does not have particle identification. *Inclusive background* consists of the combination of hadron tracks with a J/ψ coming from prompt production in the pp interaction or from decays of hadrons containing either a b or a $\bar{b}$ quark other than the B_c^+. The latter is indicated with $b\bar{b} \to J/\psi X$. The background is modeled in the official Monte Carlo production. The data sets are listed in Appendix A in Table A.

The inclusive background is dominated by b-hadron decays. It does not have a peak in the mass range of the B_c^+ reconstructed mass spectrum. It consists of the superposition of the tails of several resonances which can be well approximated by a decaying exponential function. The combinatorial background involving production of prompt J/ψ (derived from $pp \to J/\psi X$) makes the next most important contribution and has a flat spectrum in the reconstructed mass.

The background from specific decay processes is called *exclusive background*. The $B \to J/\psi K^+$ decay with the K^+ interpreted as a π^+ has some contribution in the signal region and is included in the $b\bar{b} \to J/\psi X$ sample. The other exclusive backgrounds are non-signal decay channels of the B_c^+ including a J/ψ. The $\mu^+\mu^-$ from the J/ψ decay are combined with a hadron of mass different than the π^+, or hadrons are missed by the reconstruction, leading to an incorrect measurement of the mass. In the semileptonic decay $B_c^+ \to J/\psi\nu_\mu\mu^+$, the μ^+ is assigned the pion mass and the ν energy is not detected. The $B_c^+ \to J/\psi\rho^+$ decays have a ρ^+ in the final state, which decays further into $\pi^+\pi^0$. The π^0 is missed by the reconstruction. Only one π^+ is used from the $B_c^+ \to J/\psi\pi^+\pi^0$ and $B_c^+ \to J/\psi\pi^+\pi^-\pi^+$ decays, leading to a shift towards lower reconstructed mass. Although their branching ratios are higher than the branching ratio of the $B_c^+ \to J/\psi\pi^+$, their contribution is small, because their main contribution

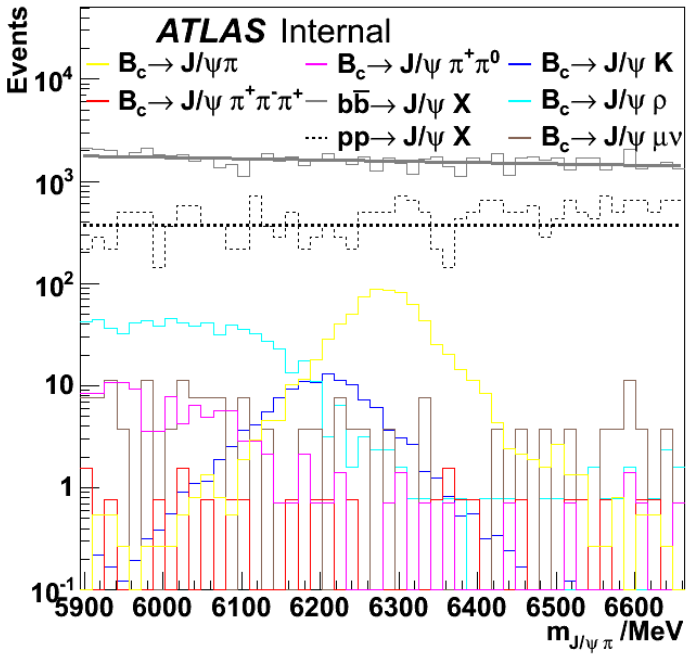

Figure 5.1: The contributions of exclusive and combinatorial backgrounds in the B_c^+ reconstructed mass spectrum (semilogarithmic scale). The $B_c^+ \to J/\psi\pi^+$ signal peak position is shown for comparison (yellow line). The prompt J/ψ background is fitted with a constant and the $b\bar{b} \to J/\psi X$ contribution with an exponential. Details of the fit results are given in the main text. The fluctuations around these fits are expected to be due to limited statistics in the Monte Carlo samples.

lies below the mass range selected for this analysis. The decay $B_c^+ \to J/\psi K^+$ is Cabibbo-suppressed, because quarks of two different generations, namely u and $\bar{s}$, are produced in the weak decay of the $\bar{b}$ to $\bar{c}$. It has thus approximately 0.05 times the amplitude of the $B_c^+ \to J/\psi\pi^+$ signal decay. Only a small shift in the reconstructed mass of these two decays can be seen, because the masses of the K^+ and the π^+ are similar. Thus, the exclusive backgrounds contribute to invariant masses below the B_c^+ mass peak.

The background contributions are illustrated in Figure 5.1 and Figure 5.2. They show that the background spectrum is mostly due to the inclusive backgrounds and the contribution from the exclusive background plays a minor role. The number of Monte Carlo events N_{MC} was scaled by luminosity (multiplication by $L^{\text{int}}\sigma \cdot BR/N_{MC}$). It represents the number of events expected in the collision data at 8 TeV center of mass energy.

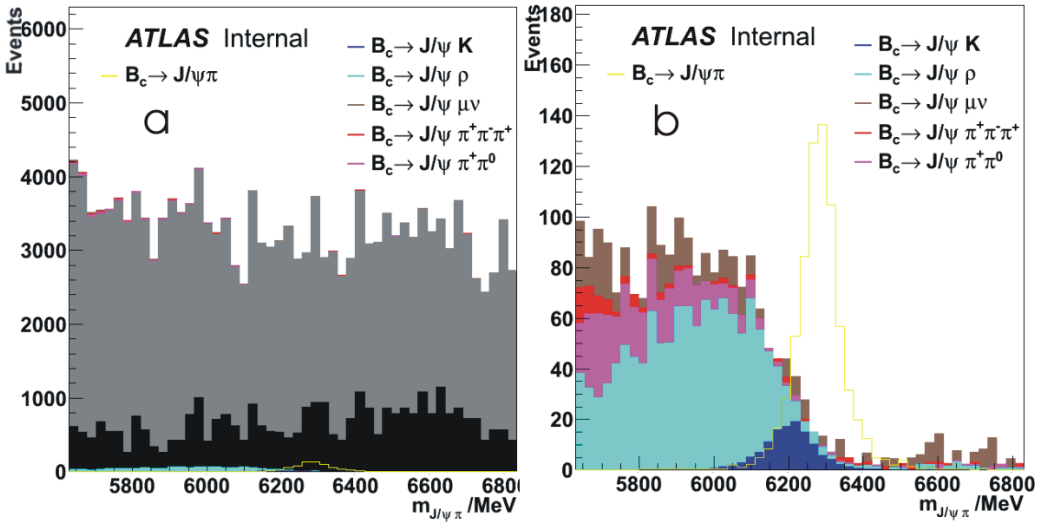

Figure 5.2: The contributions of the exclusive and combinatorial backgrounds. The $B_c^+ \to J/\psi\pi^+$ signal peak position is shown for comparison (yellow line). The left graph (a) shows the stacked contributions of both the exclusive and combinatorial background. The mass spectrum of the combined backgrounds is dominated by the inclusive background contributions. The $B \to J/\psi K^+$ contribution in this region is included in the $b\bar{b} \to J/\psi X$ background. The right graph (b) shows the stacked contributions of the exclusive backgrounds and the signal position for comparison.

The Monte Carlo data are scaled based on theoretical predictions for cross section and branching ratio. These predictions have non-negligible uncertainties. As Table 5.1 and Table 5.2 show, several theoretical models lead to different branching ratios. The biggest uncertainty on the contribution of each background type comes from the prediction of the cross section for the B_c^+ production. (The cross section predictions for the B_c^+ ground state are shown in Table 4.1.) It gives rise to an uncertainty of at least 25 % in the number of luminosity scaled Monte Carlo events for the exclusive backgrounds and the $B_c^+ \to J/\psi\pi^+$ signal. This is not a problem as long as only exclusive backgrounds are considered, but the inclusive backgrounds have different production cross sections. The prompt and b-hadron production cross

section times branching ratio were measured by CMS at $\sqrt{s} = 7\,\text{TeV}$ to be $\sigma(b\bar{b} \to J/\psi)BR(J/\psi \to \mu^-\mu^+) = (26.0 \pm 1.4_{stat} \pm 1.6_{sys} \pm 2.9_{lumi})\,\text{nb}$ and $\sigma(pp \to J/\psi)BR(J/\psi \to \mu^-\mu^+) = (70.9 \pm 2.1_{stat} \pm 3.0_{sys} \pm 7.8_{lumi})\,\text{nb}$[36] respectively. The production cross sections used in the luminosity scaling are: $\sigma(pp \to B_c^+) = 26\,\text{nb}$, $\sigma(b\bar{b} \to J/\psi) = 223\,\text{nb}$, and $\sigma(pp \to J/\psi) = 1254\,\text{nb}$. The branching ratios are displayed in Table 5.3.

BR in % as reported in:	Decays: $B_c^+ \to J/\psi X$	$B_c^+ \to J/\psi\pi^+$	$B_c^+ \to J/\psi\rho^+$	$B_c^+ \to J/\psi\pi^+\pi^0$
[37], PM		0.22	0.666	
[14], QM		0.2	0.6	
[38], SR		0.13	0.4	
[38], PM		0.08	0.2	
[39], QM	13.2	0.061	0.16	
[40], ISGW		0.1		
[41], LC		0.13	0.38	0.35
[41], QM		0.17	0.44	0.44
[41], SR		0.17	0.48	0.48
[30], SR		0.13		

Table 5.1: The branching ratio predictions for three exclusive backgrounds and the $B_c^+ \to J/\psi\pi^+$ signal as reported in several papers using different theoretical models for the calculations: quark model (QM); QCD sum rules (SR); expansions in the mass ratio $m(J/\psi)/m(B_c)$ (LC); Isgur, Scora, Grinstein, and Wise model (ISGW). Their results differ. The luminosity scaling of the Monte Carlo sample varies with the choice of the branching ratio prediction.

The $b\bar{b} \to J/\psi$ production has a lower cross section than the prompt $pp \to J/\psi$ production of the J/ψ. Nevertheless, it is the major contribution to the shape of the mass spectrum in the mass range of interest for the B_c^+ measurement. The $pp \to J/\psi$ play some role. The statistics in the mass spectrum of collision data do not allow features from the exclusive backgrounds to emerge (compare Figure 5.6).

BR in % as reported in:	Decays: $B_c^+ \to J/\psi\pi^+\pi^-\pi^+$	$B_c^+ \to J/\psi K^+$	$B_c^+ \to J/\psi\mu^+\nu$
[38], SR		0.011	
[38], PM		0.007	
[39], QM			1.7
[41], LC	0.52		
[41], QM	0.64		
[41], SR	0.48		
[30], SR		0.011	

Table 5.2: The branching ratio predictions for three exclusive backgrounds as reported in several papers using different theoretical models for the calculations: quark model (QM); QCD sum rules (SR); expansions in the mass ratio $m(J/\psi)/m(B_c)$ (LC). Their results differ. The luminosity scaling of the Monte Carlo sample varies with the choice of the branching ratio prediction.

Sample	Combined BR /%	BR /%
$B_c^+ \to J/\psi\pi^+$	0.008	0.13
$B_c^+ \to J/\psi\rho^+$	0.024	0.4
$B_c^+ \to J/\psi\pi^0\pi^+$	0.021	0.35
$B_c^+ \to J/\psi\pi^+\pi^+\pi^-$	0.023	0.39
$B_c^+ \to J/\psi K^+$	0.0007	0.011
$B_c^+ \to J/\psi\mu\nu$	0.144	1.9

Table 5.3: The branching ratios and combined branching ratios as they are used in the luminosity scaling of the different Monte Carlo samples. The combined branching ratios are the branching ratios for the decays into $J/\psi X$ times the branching ratio for the $J/\psi \to \mu^+\mu^-$ decay, $(5.93 \pm 0.06)\,\%$[35].

5.2 Reconstruction requirements

The data for this analysis are obtained from the ATLAS B-physics stream. Only data with fully operational Inner Detector and Muon Spectrometer are used in the reconstruction of the b-hadron decays. Further cuts are applied and at the same time only the events with the best vertex reconstruction (lowest χ^2/NDF) for each bunch-crossing are accepted.

	Cut
$m(J/\psi)$	$2200 \ldots 4000\,\text{MeV}$
$p_{\text{T}}(\pi^+)$	$> 500\,\text{MeV}$
$d_0(\pi^+)$	> 1
$m(B_c^+)$	$4 \ldots 8\,\text{GeV}$
$\chi^2(B_c^+)/NDF$	< 10
$\chi^2(J/\psi)/NDF$	< 10
$p_{\text{T}}(\mu_1)$	$> 6\,\text{GeV}$
$p_{\text{T}}(\mu_2)$	$> 4\,\text{GeV}$
$m(J/\psi)$	$2915 \ldots 3275\,\text{MeV}$
$p_{\text{T}}(B)$	$> 10\,\text{GeV}$
Hadron Pixel hits	> 1
Hadron SCT hits	> 4

Table 5.4: The cuts applied within the reconstruction of b-hadron decays in the study of additional selection criteria to enhance the B_c^+ yield. The parameters are explained in the text.

The cuts applied at this level are shown in Table 5.4. The cut on the transverse momentum $p_{\text{T}}(\pi^+)$ of the hadron, which is assigned to be a pion, had to be adjusted for the tuning of the cuts in 5.2.1 in order to study this cut below 3 GeV. For the study of the cuts the reconstructed data of the periods D, E, and L are used with a $p_{\text{T}}(\pi^+)$ lower threshold of 500 MeV. A list of the data sets is given in Appendix A in Table A. A similar study of the cuts has been carried out by another group for their measurement of the B_c^+ lifetime[1]. They were able to reconstruct 308 ± 50 B_c^+ decays in 2012 ATLAS data. Their cut has been chosen to be at $p_{\text{T}}(\pi^+) > 2.8\,\text{GeV}$.

The other parameters input to selections are: the transverse momenta $p_{\text{T}}(B_c^+)$, $p_{\text{T}}(\mu_1)$, and $p_{\text{T}}(\mu_2)$ of the B_c^+ meson and the two muons respectively;

[1]Steffen Maeland, Gerald Eigen, "Update on B_c^+ lifetime," talk given at the ATLAS BJPsi Subgroup meeting on January 23 2014.

and the masses $m(J/\psi)$ and $m(B_c^+)$ of the J/ψ and the B_c^+ meson. The vertex fit quality for the primary vertex (point where the B_c^+ meson is produced) and the secondary vertex (point of the B-decay) are $\chi^2(B_c^+)/NDF$ and $\chi^2(J/\psi)/NDF$ respectively. The cut on the impact parameter projection onto the plane perpendicular to the beam axis, d_0, of the π^+ is depicted in Figure 5.3. The $p_{\mathrm{T}}(\mu_1)$ and $p_{\mathrm{T}}(\mu_2)$ cuts confirm the trigger selection, whereas the other cuts lead to a reduction of data by rejecting badly reconstructed background and badly reconstructed signal events. Additionally cuts on the number of hits in the pixel and SCT detectors of the Inner Detector are applied. The selection criteria shown in Table 5.4 are confirmed by the following offline analysis.

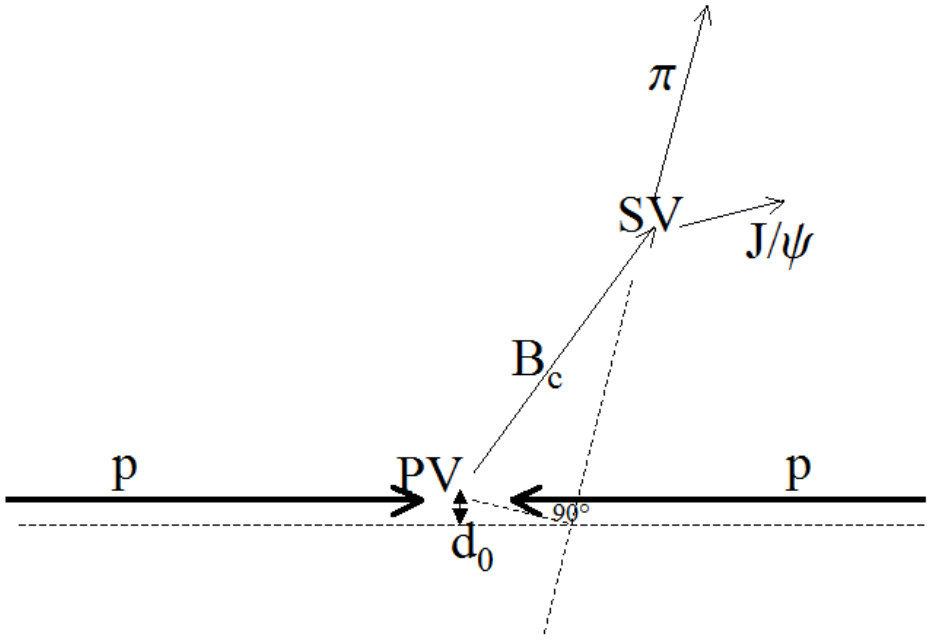

Figure 5.3: Illustration of the impact parameter projection d_0. This is the projection of the distance between the primary vertex (PV) and the π^+ momentum vector on the plane perpendicular to the beam axis. The figure also shows the secondary vertex (SV) with the decay of the B_c^+ into π^+ and J/ψ.

5.2.1 Introduction to the selection of the B_c^+ events

In the subsequent analysis, quality cuts and selection cuts are applied. The quality cuts ensure a sufficient number of detector hits for the hadrons and muons, successful reconstruction of both muons, and a good vertex fit for the J/ψ. For the hadrons it is required that the tracks do not have any holes in the pixel and SCT detectors of the ID[42], which means that all active detector elements intersected by the track must be responsive. The sum of the pixel and SCT hits is required to be bigger than eight[42]. The requirements in the pixel detector and SCT ensure a reliable impact parameter reconstruction for the pion and kaon. The muons must have more than six hits in the SCT, which is stricter than recommended by the Muon Combined Performance Working Group[43], and at least one hit in the pixel detector as recommended[43].

The selection cuts optimize the B_c^+ observation by reducing the background while keeping as much signal as possible. These are: the ratio between the impact parameter projection of the π^+ and its uncertainty, $d_0(\pi^+)/\sigma(d_0)_{\pi^+}$ (d_0-significance); the vertex fit quality of the B meson, $\chi^2(B_c^+)/NDF$; and the transverse momenta $p_{\mathrm{T}}(B_c^+)$ and $p_{\mathrm{T}}(\pi^+)$ of the B_c^+ and the π^+ respectively.

A cut on $d_0(\pi^+)$ reduces the background from combinations of real J/ψ candidates with random kaons or pions which are not associated with the decay to J/ψ. The d_0-significance takes the track-by-track uncertainty $\sigma(d_0)_{\pi^+}$ into account by using it as a weight for the impact parameter projection $d_0(\pi^+)$. In a similar way restrictions on the vertex fit quality $\chi^2(B_c^+)/NDF$ ensure that only track combinations which have a high probability of coming from the same B_c^+ decay vertex are used. The cuts on the transverse momenta $p_{\mathrm{T}}(B_c^+)$ and $p_{\mathrm{T}}(\pi^+)$ help to reduce the exclusive backgrounds as well. The hadron combined with the J/ψ in the exclusive backgrounds has either a higher mass than the π^+ or there are undetected particles. In the latter case the hadron has reduced momentum due to energy conservation. Placing a minimum on the transverse momenta of the B_c and the π^+ candidate can thus reduce both the inclusive backgrounds and the exclusive backgrounds.

An additional cut on the angle between the transverse momentum of the J/ψ and the π^+ (opening angle) has been studied using the full $19.2\,\mathrm{fb}^{-1}$ of 2012 $\sqrt{s} = 8\,\mathrm{TeV}$ data. It is found to lead to an artificial mass shift. Consequently, this cut is not used. The results of that study are shown in Figure 5.4. The fit of the B^+ mass distribution with a maximum likelihood function is explained

in Section 6, including the fitting models for the signal and the background. It yields a different value with and without the opening angle cut. The difference for an opening angle cut of $> 0.4\,\text{rad}$ is $(1 \pm 0.5_{\text{stat}})\,\text{MeV}$. Also opening angle cuts of $> 0.1\,\text{rad}$, $> 0.2\,\text{rad}$ and $0.3\,\text{rad}$ have been tested and lead to shifts towards higher masses as well. All other cuts have been applied as in [5].

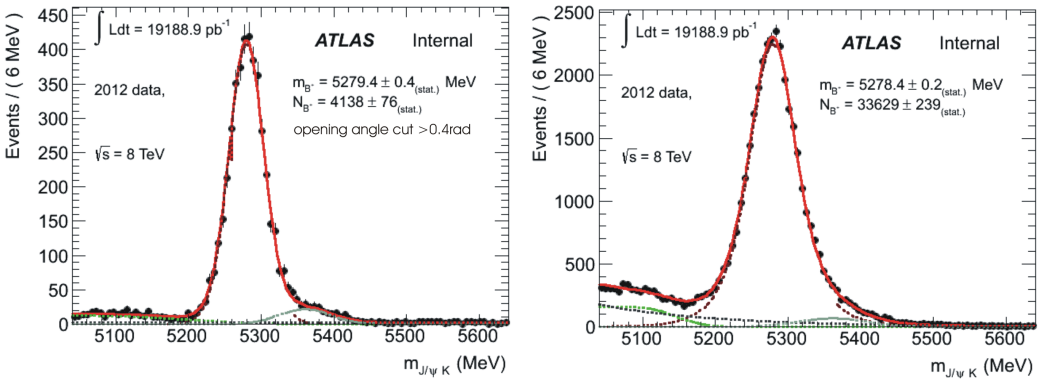

Figure 5.4: The fit for the B^+ mass distribution is shifted by about 1 MeV on the left plot, where an opening angle cut $> 0.4\,\text{rad}$ is applied, compared to the mass peak without an opening angle cut on the right.

The challenge with the remaining four selection cuts is that they are not uncorrelated. For example the transverse momenta of the π^+ and B_c^+ depend on one another due to momentum conservation. This is illustrated in Figure 5.5 for the $B_c^+ \to J/\psi\pi^+$ Monte Carlo signal and the (dominant) $b\bar{b} \to J/\psi X$ Monte Carlo background. An iterative procedure is chosen to deal with the correlations. First one cut is optimized. Its optimum value is applied before optimizing the next one. After all (four) cuts have been optimized in this manner, the procedure starts again with the first cut, while all the other optimized cuts are applied, leading finally to convergence to the final selection criteria. Afterwards the result is confirmed by repeating this procedure with a different order of the cuts.

The cut optimization could not be performed with Monte Carlo background samples due to lack of statistics. Applying the cuts from [5] leaves only a single event from the dominant $b\bar{b} \to J/\psi X$ Monte Carlo background sample in the B_c^+ mass range. The influence of the choice of cuts on this background can consequently not be examined using Monte Carlo samples. A Monte Carlo production with more events is not feasible within the time available.

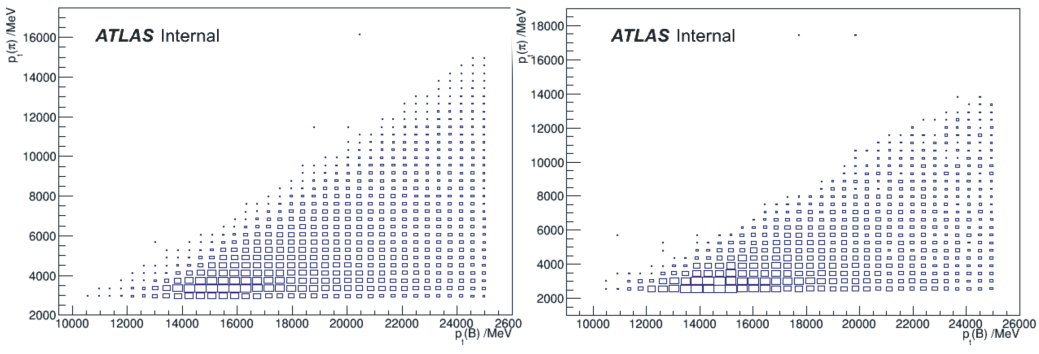

Figure 5.5: Scatter plots of $p_{\mathrm{T}}(B_c^+)$ as a function of $p_{\mathrm{T}}(\pi^+)$ for the Monte Carlo signal channel $B_c^+ \to J/\psi\pi^+$ on the left and the (dominant) background $b\bar{b} \to J/\psi X$ on the right. The size of a box represents the number of events in that bin. The signature of the conservation of momentum is visible in the triangular shape.

5.2.2 A data driven method

Data, on the other hand, give much better statistics for the background events. However, a distinction among the different background processes is *a priori* not possible. For the optimization of the cuts, an approach has been chosen which extracts the background from 2012 ATLAS data and compares it with the Monte Carlo signal sample for the $B_c^\pm \to J/\psi\pi^\pm$ decay. For the $B_c^+ \to J/\psi\pi^+$ Monte Carlo signal, truth matching is applied. This means that only the reconstructed particle with the smallest distance to the generated ("truth") particle is used.

The background is extracted from regions of invariant mass below and above the signal region in the data. These regions are referred to as the *sidebands*. The sideband with lower mass is the left sideband and the sideband with higher mass is the right sideband. They need to be combined in a way which best represents the background which is expected in the signal region. This can be done by either choosing symmetric sidebands and summing them with different weights, or by defining asymmetric sidebands. Here the second approach is chosen, because it does not create artificial events, which might reduce the resolution.

The dominant background contributions are given by the inclusive channels $b\bar{b} \to J/\psi X$ and $pp \to J/\psi X$. These backgrounds can be modeled in the reconstructed mass spectrum by $f(m_{J/\psi\pi^+}) = p_0 + \exp\left(p_1 + p_2 \cdot m_{J/\psi\pi^+}\right)$ where p_0

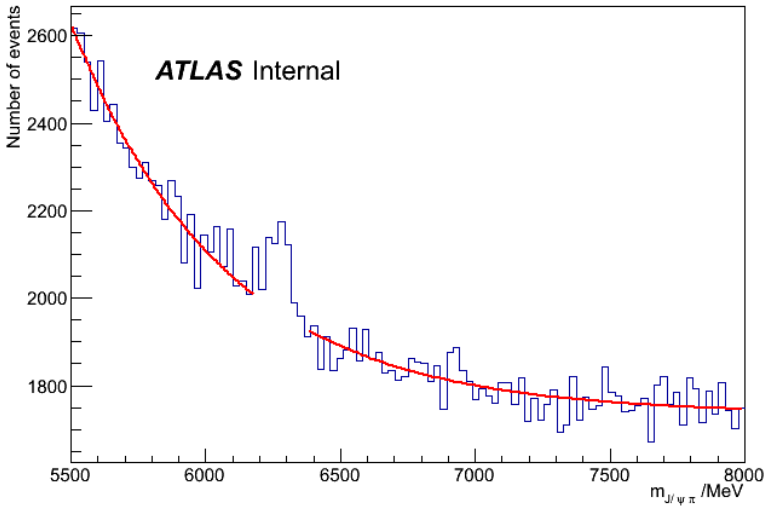

Figure 5.6: The fit of $p_0+\exp(p_1+p_2\cdot m(B_c^+))$ to the mass distribution excluding the signal region of the B_c^+ peak. It gives $p_0 = 9.1 \pm 0.5$, $p_1 = 12.13 \pm 0.03$, and $p_2 = (-1.538 \pm 0.004)\,10^{-3}\,\mathrm{MeV}^{-1}$. The quality of the fit is given by $\chi^2/ndf = 115.8/89$.

represents the contribution from the prompt J/ψ and the exponential function (with $p_2 < 0$) the contribution from the decay of B-hadrons. This function is fitted to the full $19.2\,\mathrm{fb}^{-1}$ of 2012 ATLAS data with $\sqrt{s} = 8\,\mathrm{TeV}$, excluding the signal region. Only very loose cuts are used representing the reconstruction requirements $p_\mathrm{T}(B_c^+) > 10\,\mathrm{GeV}$, $p_\mathrm{T}(\pi^+) > 3\,\mathrm{GeV}$, $\chi^2(B_c^+)/NDF < 10$, $d_0(\pi^+)/\sigma(d_0) > 2$.

The fit minimizes the $\chi^2 = \sum_{i=1}^{N} \left(N_i - f\left(m^i_{J/\psi\pi^+}\right)\right)^2/\sigma_i^2$ function, summing over the quadratic difference of the bins $i = 1 \ldots N$ between the number of events N_i in bin i and the value of the fit model for the same bin $f\left(m^i_{J/\psi\pi^+}\right)$ at the corresponding invariant mass $m^i_{J/\psi\pi^+}$ weighted by the standard deviation σ_i. The fit is shown in Figure 5.6.

The signal region is chosen to be $\pm 3\sigma$ around the B_c^+ mass, where $\sigma = 48\,\mathrm{MeV} \pm 3\,\mathrm{MeV}$ is the width of a Gaussian peak fit to the $B \to J/\psi\pi^+$ (luminosity scaled) Monte Carlo sample, which minimizes the corresponding χ^2-function, after the selection cuts from the observation[5] have been applied. The Gaussian fit is justified because the shape of the signal distribution is dominated by the resolution of the detector. The resolution of the detector follows a Gaussian profile to a good approximation[9]. The fit is shown in Figure 5.7. The

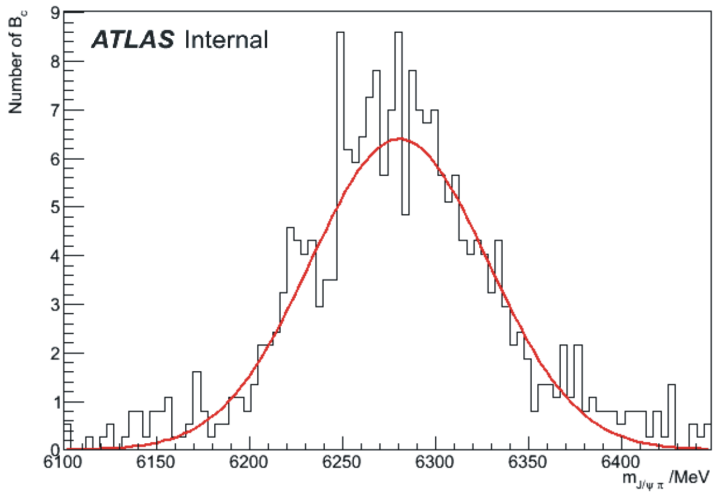

Figure 5.7: The mass distribution of a luminosity scaled Monte Carlo $B_c^+ \to J/\psi\pi^+$ sample fitted with a Gaussian function has a width of $\sigma = (47.69 \pm 3.38)$ MeV. The mean is given by (6280 ± 3.5) MeV, and the fit quality is $\chi^2/ndf = 23.34/81$.

B_c^+ mass returned by the fit is consistent with the $M_{B_c^+} = (6277\,\text{MeV} \pm 6)\,\text{MeV}$ 2012 world average value[15]. (The new world average value for the B_c^+ mass is (6274.5 ± 1.8) MeV[44].) The fit results of Figure 5.6 are confirmed with an unbinned maximum likelihood fit (see Section 6).

The number of background events in the signal region is estimated by

$$B_S = p_0 \cdot 6\sigma + \exp(p_1) \cdot \int_{M_{B_c^+}-3\sigma}^{M_{B_c^+}+3\sigma} \exp\left(p_2 \cdot m_{J/\psi\pi^+}\right) \mathrm{d}m_{J/\psi\pi^+}. \tag{5.1}$$

The background in the sidebands is expected to be

$$B_L = p_0 \cdot (n_1\sigma - 5\sigma) - \exp(p_1) \cdot \int_{M_{B_c^+}-5\sigma}^{M_{B_c^+}-n_1\sigma} \exp\left(p_2 \cdot m_{B_c^+}\right) \mathrm{d}m_{J/\psi\pi^+} \tag{5.2}$$

in the left (lower reconstructed mass) sideband and

$$B_R = p_0 \cdot (n_2\sigma - 5\sigma) + \exp(p_1) \cdot \int_{M_{B_c^+}+5\sigma}^{M_{B_c^+}+n_2\sigma} \exp\left(p_2 \cdot m_{J/\psi\pi^+}\right) \mathrm{d}m_{J/\psi\pi^+} \tag{5.3}$$

in the right (higher reconstructed mass) sideband. The n_1 and n_2 are the outer sideband boundaries as multiples of σ. The requirement to represent

the constant background in the signal region leads to the condition that $n_1\,\sigma - 5\,\sigma + n_2\,\sigma - 5\,\sigma = 6\,\sigma$. Additionally the sum of the second term on the right hand sides in (5.2) and (5.3) has to be identical to the second term of the right hand side in (5.1). This leads to: $n_1 \approx 7.4$ and $n_2 \approx 8.6$. In the following section the data extracted from the region of reconstructed mass $M_{B_c^+} - 7.4\sigma \ldots M_{B_c^+} - 5\sigma$ will be referred to as the left sideband and the data extracted from $M_{B_c^+} + 5\sigma \ldots M_{B_c^+} + 8.6\sigma$ will be called the right sideband. The data sets of Periods D, E, and L are used (Appendix A, Table A).

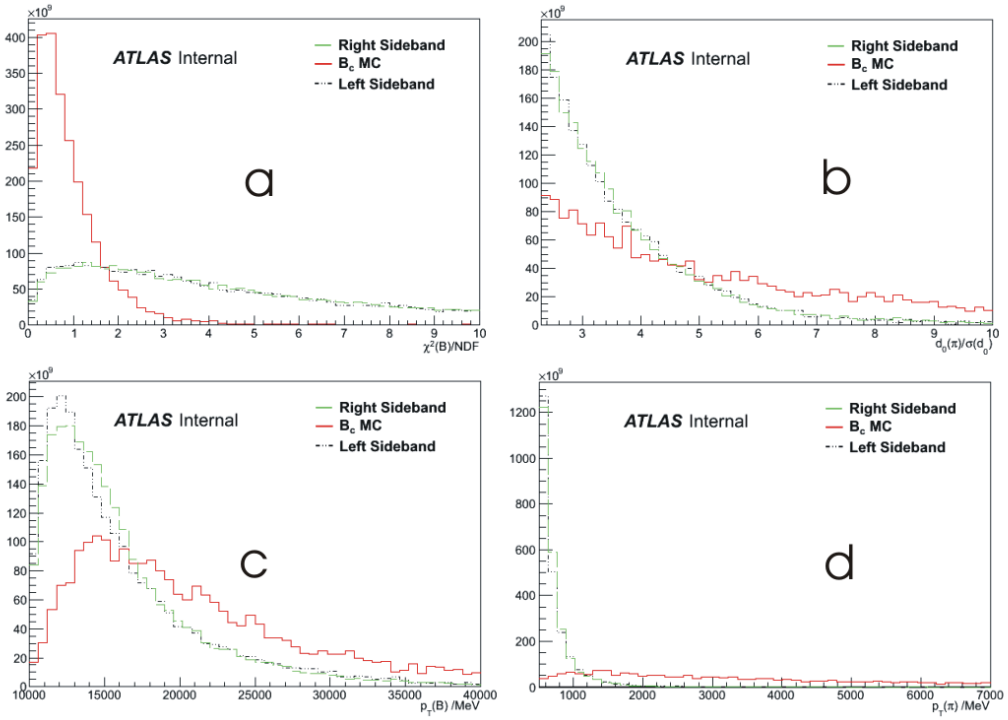

Figure 5.8: The distribution of the selection criteria: $\chi^2(B_c^+$ (a), and $d_0(\pi^+)/\sigma(d_0)$ (b), $p_{\mathrm{T}}(B_c^+)$ (c), $p_{\mathrm{T}}(\pi^+)$ (d). The Monte Carlo signal channel is displayed in red and the sidebands for Periods D, E, and L are shown in green and black. They are scaled to identical numbers of events.

The distributions of the number of events as a function of each of the four selection parameters can be used to distinguish between signal and background. The signal and the sidebands have different distributions in these parameters. They are shown in Figure 5.8. Sidebands and Monte Carlo are scaled to have the same number of entries. These distributions allow for an initial estimate

of the cut position. Regions of the distributions where the background is high compared to the signal shall be excluded from the measurement. A region of interest for further optimization can be found where a distribution shows good background suppression with only small signal loss.

In this region an optimization using a figure of merit given by

$$F = \frac{S^{\text{scaled}}}{\sqrt{S^{\text{scaled}} + L + R}} \tag{5.4}$$

is performed. Here, S^{scaled} gives the number of scaled (Monte Carlo) signal events which pass the cuts and L, R are the corresponding background events in the left and right sideband of the data respectively. The scaling of the Monte Carlo events ensures that the number of signal events observed in the full 2012 data, with the cuts as in [5], and in the $B_c^+ \to J/\psi\pi^+$ Monte Carlo sample, are identical. Afterwards it is corrected for the luminosity. The data from Periods D, E, and L have an integrated luminosity $L^{\text{int}}_{DEL} = 6551.11\,\text{pb}^{-1}$. The full 2012 data set has $L^{\text{int}}_{2012} = 19.2\,\text{fb}^{-1}$. The luminosity estimation has an uncertainty of about 3.9 %[45]. This requires a down-scaling of the number of events S produced in the Monte Carlo simulation, $S^{scaled} = S \cdot 0.259 \cdot L^{\text{int}}_{DEL}/L^{\text{int}}_{2012}$.

A good set of cuts maximizes the figure of merit (5.4). The maximum of (5.4) is extracted from the figure of merit plots, such as those shown in Figure 5.9, for one parameter at a time. Further optimization is done in an iterative manner as described before. This is done twice in different orders: $p_{\text{T}}(B_c^+)$, $p_{\text{T}}(\pi^+)$, $\chi^2(B_c^+)/NDF$, $d_0(\pi^+)/\sigma(d_0)$ and $\chi^2(B_c^+)/NDF$, $p_{\text{T}}(\pi^+)$, $p_{\text{T}}(B_c^+)$, $d_0(\pi^+)/\sigma(d_0)$, leading to consistent results. The very loose cuts, $p_{\text{T}}(\pi^+) > 500\,\text{MeV}$, $p_{\text{T}}(B_c^+) > 10\,\text{GeV}$, $\chi^2(B_c^+)/NDF < 10$, and $d_0(\pi^+)/\sigma(d_0) > 2$, are used as a starting point. The corresponding figure of merit plots for the optimization starting with $\chi^2(B_c^+)/NDF$ are shown in Figure 5.9. At the same time the figure of merit using only a left sideband $M_{B_c^+} - 7\sigma \ldots M_{B_c^+} - 5\sigma$ shows that the choice of the sidebands has only a small influence on the results. The figure of merit is then given by

$$F_1 \propto S^{\text{scaled}}/\sqrt{S^{\text{scaled}}/3 + L_1}, \tag{5.5}$$

where L_1 is the number of events in the left sideband. The cross-check single sideband optimization is shown in Figure 5.10. The exclusive backgrounds

present in the left sideband play no significant role in the figure of merit optimization.

The cuts that specify the dataset for analysis, and are applied subsequently to the track quality cuts and the cuts confirming reconstruction requirements, are:

$$p_{\mathrm{T}}(B_c^+) > 13\,\mathrm{GeV}, \tag{5.6}$$

$$p_{\mathrm{T}}(\pi^+) > 3.2\,\mathrm{GeV}, \tag{5.7}$$

$$\frac{\chi^2(B_c^+)}{NDF} < 2.8, \tag{5.8}$$

$$\frac{d_0(\pi^+)}{\sigma(d_0)} > 2.6. \tag{5.9}$$

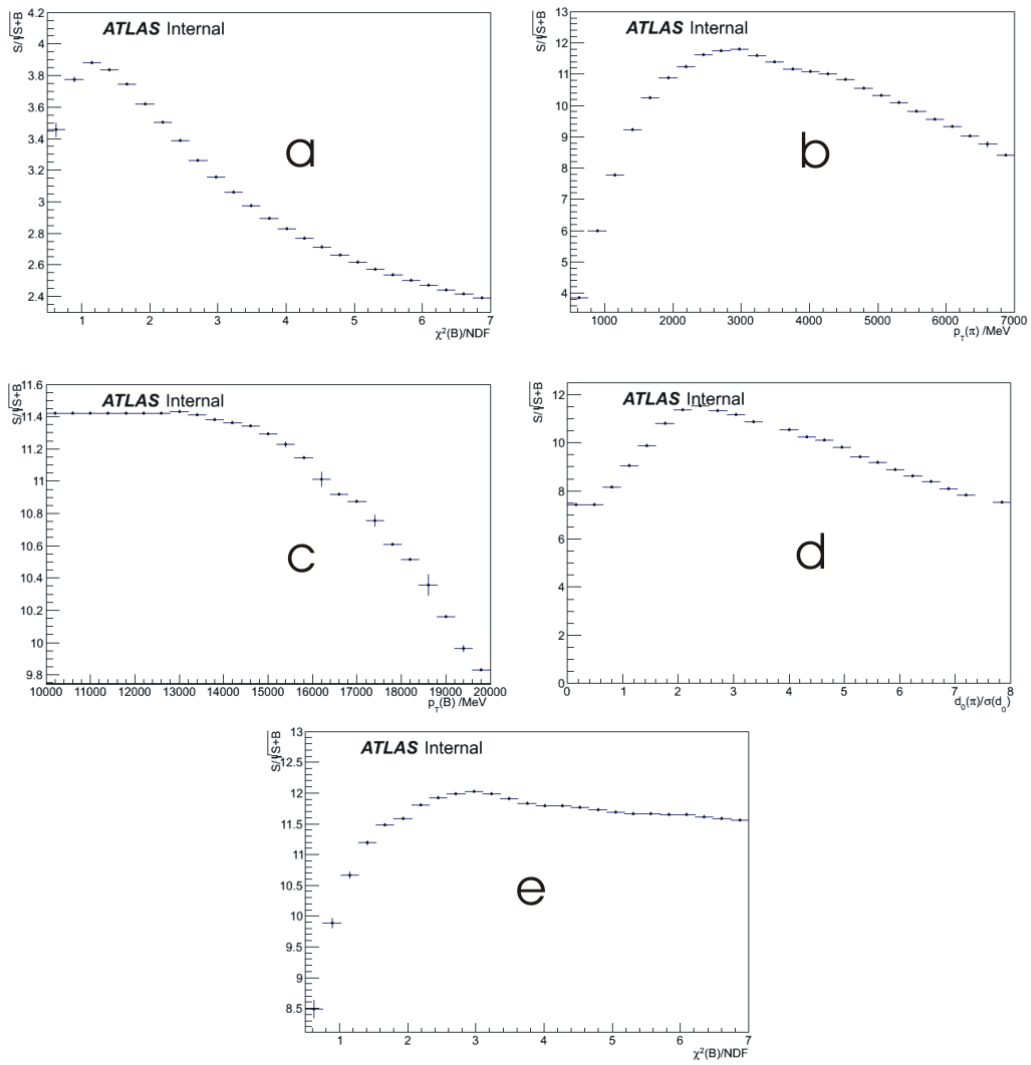

Figure 5.9: The figure of merit (Equation 5.4) versus the selection cuts for each step of the maximization. First $\chi^2(B_c^+)/NDF$ is optimized (a). A maximum can be seen at $\chi^2(B_c^+)/NDF \approx 1.4$. The maximum for the $p_{\mathrm{T}}(\pi^+)$ plot (b) with $\chi^2(B_c^+)/NDF < 1.4$ is found to be at $p_{\mathrm{T}} \approx 3.2\,\mathrm{GeV}$. The maximum for the $p_{\mathrm{T}}(B_c^+)$ plot (c) with $\chi^2(B_c^+)/NDF < 1.4$ and $p_{\mathrm{T}} > 3.2\,\mathrm{GeV}$ is found to be at $p_{\mathrm{T}}(B_c^+) \approx 13\,\mathrm{GeV}$. The maximum for the $d_0(\pi^+)/\sigma(d_0)$ plot (d) with $\chi^2(B_c^+)/NDF < 1.4$, $p_{\mathrm{T}} > 3.2\,\mathrm{GeV}$, and $p_{\mathrm{T}}(B_c^+) > 13\,\mathrm{GeV}$ is found to be at $d_0(\pi^+)/\sigma(d_0) \approx 2.6$. The maximum for the $\chi^2(B_c^+)/NDF$ plot (e) with $p_{\mathrm{T}} > 3.2\,\mathrm{GeV}$, $p_{\mathrm{T}}(B_c^+) > 13\,\mathrm{GeV}$, and $d_0(\pi^+)/\sigma(d_0) > 2.6$ is found to be at $\chi^2(B_c^+)/NDF < 2.8$. The selection criteria have converged towards (5.6) - (5.9).

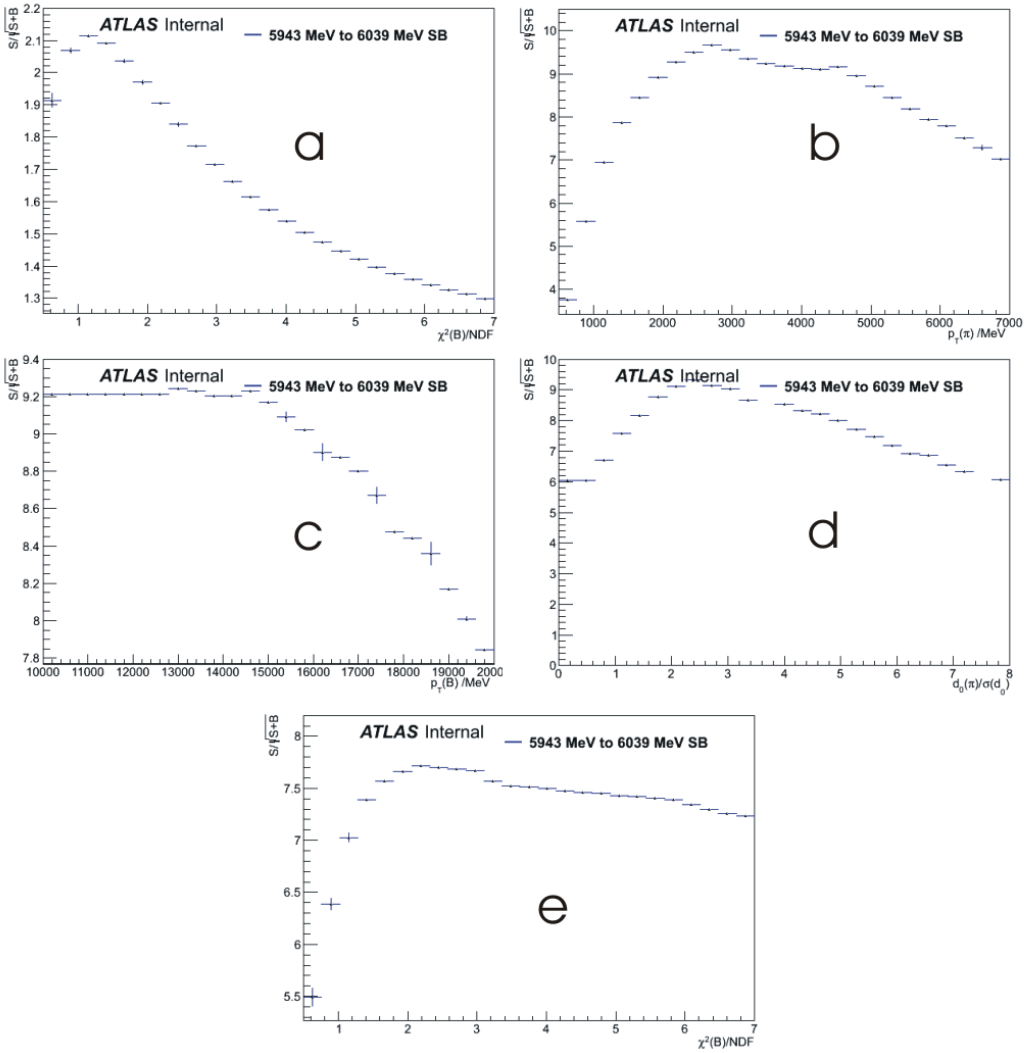

Figure 5.10: The figure of merit (Equation 5.5) versus selection parameters using only a left sideband analogous to those shown in Figure 5.9. The optimization process leads to the same selection criteria as are shown in Figure 5.9.

6 The Relative Cross Section

In this and the following chapters the notation of $B_c^{\pm}$ and $B^{\pm}$ will be used when no distinction between the charge states is made.

The cuts are applied in the measurement of the relative production cross section times branching ratio given by

$$\frac{\sigma(B_c^{\pm})}{\sigma(B^{\pm})} \cdot \frac{BR(B_c^{\pm} \to J/\psi\pi^{+})}{BR(B^{\pm} \to J/\psi K^{\pm})} \cdot \frac{BR(J/\psi \to \mu^{+}\mu^{-})}{BR(J/\psi \to \mu^{+}\mu^{-})} = \frac{N(B_c^{\pm})}{N(B^{\pm})}. \tag{6.1}$$

The numbers of $B_c^{\pm}$ and $B^{\pm}$ events are given by $N(B_c^{\pm})$ and $N(B^{\pm})$ respectively. In this measurement the charge states are treated identically when the yields are extracted. Thus, the sums of the contributions of both charge states, $N^{\mathrm{reco}}(B_c^{+}) + N^{\mathrm{reco}}(B_c^{-})$ and $N^{\mathrm{reco}}(B^{+}) + N^{\mathrm{reco}}(B^{-})$, are measured. The numbers of events $N(B_c^{\pm})$ and $N(B^{\pm})$ can not be measured directly, but can be inferred from the numbers of reconstructed events, which are obtained from the fits to the invariant mass spectra as described in section 6.1. These shall be corrected for the efficiencies of the detector response and the choice of selection criteria as reported in section 6.2:

$$N(B_c^{\pm}) = \frac{N^{\mathrm{reco}}(B_c^{+}) + N^{\mathrm{reco}}(B_c^{-})}{A(B_c^{\pm}) \cdot (\epsilon(B_c^{+}) + \epsilon(B_c^{-}))}, \tag{6.2}$$

$$N(B^{\pm}) = \frac{N^{\mathrm{reco}}(B^{+}) + N^{\mathrm{reco}}(B^{-})}{A(B^{\pm}) \cdot (\epsilon(B^{+}) + \epsilon(B^{-}))}. \tag{6.3}$$

The detector response is factorized in the acceptance $A(B_c^{+})$, $A(B^{+})$ and the efficiencies for both charge states including the efficiency of the selection criteria $\epsilon(B^{+}) + \epsilon(B^{-})$, $\epsilon(B_c^{+}) + \epsilon(B_c^{-})$. It can be shown from the condition $N^{\mathrm{reco}}(B_c^{+})/\epsilon(B_c^{+}) = N^{\mathrm{reco}}(B_c^{-})/\epsilon(B_c^{-})$ that the sum of the efficiencies for both charge states has to be used. The same applies to $N^{\mathrm{reco}}(B^{\pm})$ and the $B^{\pm}$ meson. Using (6.2) and (6.3), the relative cross section (6.1) can be calculated from the

measurements

$$\frac{\sigma(B_c^\pm)}{\sigma(B^\pm)} \cdot \frac{BR(B_c^\pm \to J/\psi\pi^\pm)}{BR(B^\pm \to J/\psi K^\pm)} = \left[\frac{1}{A(B_c^\pm)} \frac{N^{\text{reco}}(B_c^+) + N^{\text{reco}}(B_c^-)}{\epsilon(B_c^+) + \epsilon(B_c^-)}\right] \Bigg/ \left[\frac{1}{A(B^\pm)} \frac{N^{\text{reco}}(B^+) + N^{\text{reco}}(B^-)}{\epsilon(B^+) + \epsilon(B^-)}\right]. \tag{6.4}$$

This number is measured for two bins in p_{T} in the barrel region of the inner detector ($|\eta| < 1.05$). The binning in the barrel region is selected so that the number of reconstructed $B_c^\pm$ events, $N^{\text{reco}}(B_c^+) + N^{\text{reco}}(B_c^-)$, is balanced. An initial estimation of the bin boundaries is made using the $B_c^\pm \to J/\psi\pi^\pm$ Monte Carlo sample. The binning is confirmed and refined by fitting to the invariant mass distribution of the $B_c^\pm$ in the proposed bins, ensuring a successful fit and sufficient resolution. The fitting procedures are described in the next sections. The bin boundaries are: $13\,\text{GeV} < p_{\text{T}}(B_c^\pm) < 22\,\text{GeV}$ and $p_{\text{T}}(B_c^\pm) \geq 22\,\text{GeV}$. They are also applied to the $B^\pm$: $13\,\text{GeV} < p_{\text{T}}(B^\pm) < 22\,\text{GeV}$ and $p_{\text{T}}(B^\pm) \geq 22\,\text{GeV}$.

6.1 Signal yield

The yields of the $B_c^\pm$ and $B^\pm$ are calculated from unbinned maximum likelihood fits to the invariant mass distributions in each bin in p_{T}. The method is similar to the ones used in [5; 46]. It involves calculating the parameters which maximize the *likelihood function*, defined as

$$\mathcal{L} = \prod_{i=1}^{N} \left[f_{signal}\mathcal{F}_{signal}(m^i_{J/\psi X}) + (1 - f_{signal})\mathcal{F}_{bkg}(m^i_{J/\psi X})\right] \tag{6.5}$$

where N is the total number of $J/\psi X$ candidates, with $X = \pi^\pm$ for the $B_c^\pm$ and $X = K^\pm$ for the $B^\pm$, and f_{signal} is the fraction of the signal in the total number of events. The contribution from the signal $\mathcal{F}_{signal}$ is modeled by a multi-Gaussian density distribution. It is given by

$$\mathcal{F}_{signal}(m^i_{J/\psi\pi}) \propto \exp\left(-\frac{(m^i_{J/\psi\pi} - M_{B_c^\pm})^2}{2s\delta m^i_{J/\psi\pi}}\right) \tag{6.6}$$

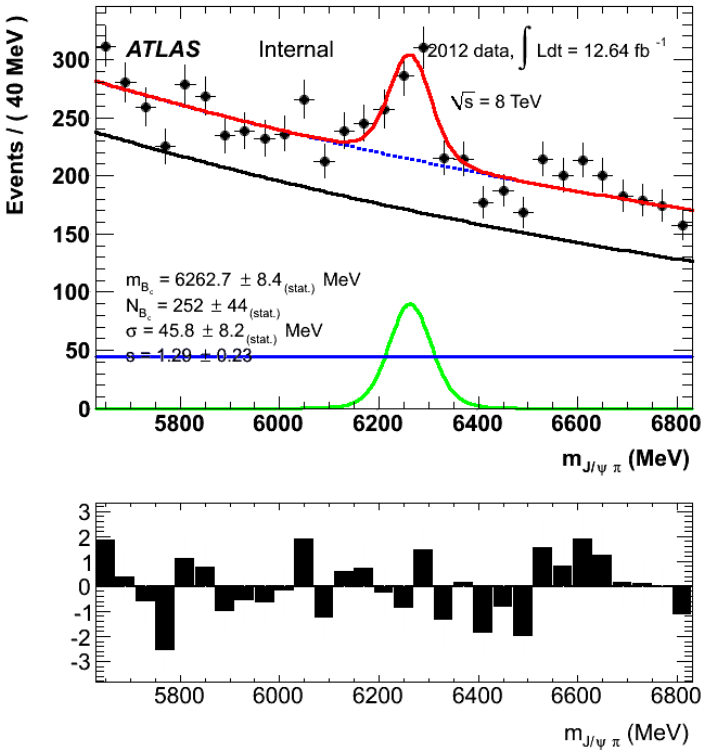

Figure 6.1: The fit of the invariant mass distribution for the $B_c^\pm$ meson for $p_\mathrm{T}(B_c^\pm) > 13\,\mathrm{GeV}$. The $B_c^\pm$ mass measured by the ATLAS detector is $M_{B_c^\pm} = (6262.7 \pm 8.4_\mathrm{stat})\,\mathrm{MeV}$. It is used to constrain the mass in the fits in both $p_\mathrm{T}(B_c^\pm)$ bins. The pull plot below shows the deviation between the fit model and data in multiples of their standard deviation.

for the $B_c^\pm$ and by

$$\mathcal{F}_{signal}(m^i_{J/\psi K^\pm}) \propto \exp\left(-\frac{(m^i_{J/\psi K^\pm} - M_{B^\pm})^2}{2s\delta m^i_{J/\psi K^\pm}}\right) \tag{6.7}$$

for the $B^\pm$, where $M_{B^\pm}$ and $M_{B_c^\pm}$ are the masses of the $B^\pm$ and $B_c^\pm$ respectively. $M_{B^\pm}$ is taken as a free parameter in the fit over the range $[5.082\,\mathrm{GeV}; 5.54\,\mathrm{GeV}]$. $M_{B_c^\pm}$ is taken as a free parameter in the range of the fit $[5.63\,\mathrm{GeV}; 6.83\,\mathrm{GeV}]$. This fit uses all events with $p_\mathrm{T}(B_c^\pm) > 13\,\mathrm{GeV}$. It is shown in Figure 6.1. For the fits in the bins in $p_\mathrm{T}(B_c^\pm)$, $M_{B_c^\pm}$ is constrained to $[6.254\,\mathrm{GeV}; 6.271\,\mathrm{GeV}]$. The range is specified by the result $M_{B_c^\pm} = (6262.7 \pm 8.4)\,\mathrm{MeV}$ from the fit using the whole $p_\mathrm{T}(B_c^\pm) > 13\,\mathrm{GeV}$ range and $M_{B_c^\pm} \in [5.63\,\mathrm{GeV}; 6.83\,\mathrm{GeV}]$. This is done to avoid fluctuations due to low statistics, taking into account that $M_{B_c^\pm}$

is independent of the transverse momentum. The world average values [15; 18] are not used due to the ATLAS energy scale offset, which is $\approx 0.7\,\text{MeV}$ for the $B^{\pm}$ and probably similar for the $B_c^{\pm}$. The widths $s\delta m^i_{J/\psi\pi^{\pm}}$, $s\delta m^i_{J/\psi K^{\pm}}$ are the product of the scale factor s and event by event mass resolution, where the scale factor accounts for differences between per-event errors on the candidate masses and the overall mass resolution. Ideally the value of s is one.

The background contributions $\mathcal{F}_{bkg}$ in the mass regions of the $B_c^{\pm}$ and the $B^{\pm}$ are different. The background of the $B_c^{\pm}$ is modeled with an exponential function plus a constant contribution

$$\mathcal{F}_{bkg} \propto \exp(a \cdot m^i_{J/\psi\pi^{\pm}}) + b. \tag{6.8}$$

Both the model of the sum of all background contributions and the signal model are normalized to unity within the mass range of the fit. Thus this fit has four free parameters: $M_{B_c^{\pm}}$, s, a, and b plus the signal fraction f_{signal}.

In the $B^{\pm}$ mass region there are further background contributions modeled by the background model $\mathcal{F}_{bkg}(m^i_{J/\psi K^{\pm}})$. The partially reconstructed b-hadron decays, where not all final hadrons are observed, contribute only to masses below the $B^{\pm}$ mass because of the missing energy. Their contributions are estimated with a complementary error function

$$\mathcal{F}^1_{bkg}(m^i_{J/\psi K^{\pm}}) \propto 1 - \operatorname{erf}\left(\frac{m^i_{J/\psi K^{\pm}} - m_0}{s_0}\right) = 1 - \frac{2}{\sqrt{\pi}} \int\limits_{\frac{m^i_{J/\psi K^{\pm}} - m_0}{s_0}}^{\infty} e^{-t^2}\,\mathrm{d}t \tag{6.9}$$

where m_0, s_0 determine the position and the slope of the error function respectively.

The Cabibbo-suppressed decay $B^{\pm} \to J/\psi\pi^{\pm}$ has a contribution to the right (towards higher masses) of the invariant mass peak of the $B^{\pm}$, when the $\pi^{\pm}$ is wrongly assigned the higher mass of the $K^{\pm}$ leading to an overestimation of the energy. It is modeled by a multi-Gaussian function

$$\mathcal{F}^2_{bkg}(m^i_{J/\psi K^{\pm}}) \propto \exp\left(-\frac{m^i_{J/\psi K^{\pm}} - M_{B^{\pm},\pi}}{2 s_1 \delta m^i_{J/\psi K^{\pm}}}\right). \tag{6.10}$$

The maximum value is fixed to $M_{B^{\pm},\pi^{\pm}} = 5360\,\text{MeV}$.

The remaining background is mostly due to production of J/ψ from b-hadrons other than the B^+, which are combined with some hadron track. They are described with an exponential function

$$\mathcal{F}^3_{bkg}(m^i_{J/\psi K^\pm}) \propto \exp\left(a \cdot m^i_{J/\psi K^\pm}\right). \tag{6.11}$$

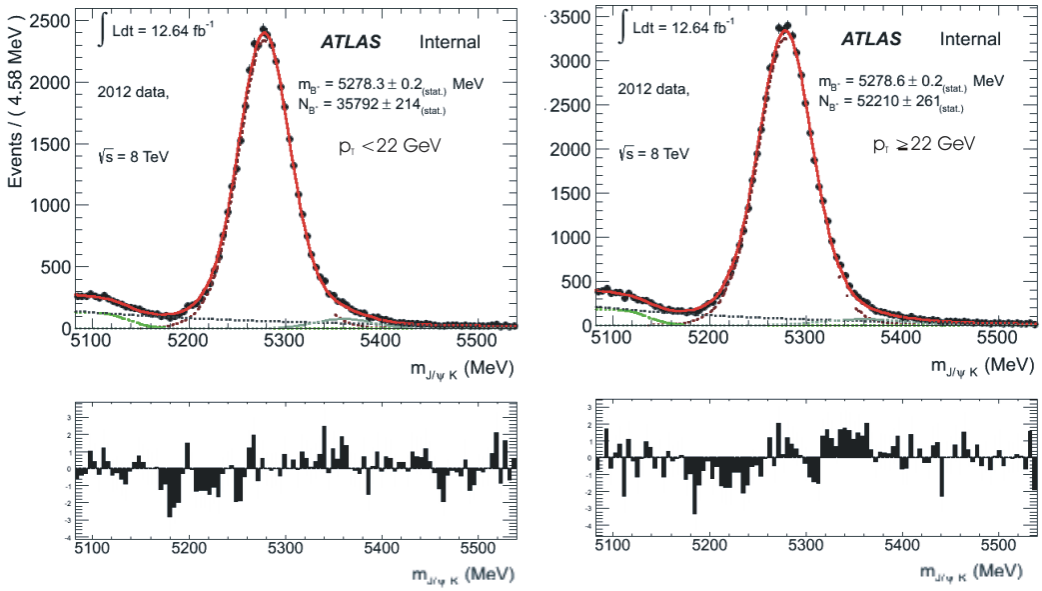

Figure 6.2: The fit of the invariant mass distribution for the $B^\pm$ meson. The fit for the low transverse momentum bin ($13\,\text{GeV} < p_\text{T}(B^\pm) < 22\,\text{GeV}$) is shown on the left, while that for the high transverse momentum bin ($p_\text{T}(B^\pm) \geq 22\,\text{GeV}$) is shown on the right. The fits are used to extract $N^\text{reco}(B^+) + N^\text{reco}(B^-)$ and its uncertainty in each bin. The pull plots below show the deviation of the data from the fit model in units of standard deviations.

The models for the different background contributions (6.9), (6.10), (6.11) are added with different weights which are optimized in the fitting procedure. The result is normalized to unity within the $B^\pm$ mass region in order to form the background model $\mathcal{F}_{bkg}(m^i_{J/\psi K^\pm})$ in (6.5). The free parameters are thus $M_{B^\pm}$, s, a, m_0, s_1, $M_{B^\pm,\pi^\pm}$, and s_0 plus the signal fraction f_{signal} and the fractions describing the relative contributions of the four different background constituents.

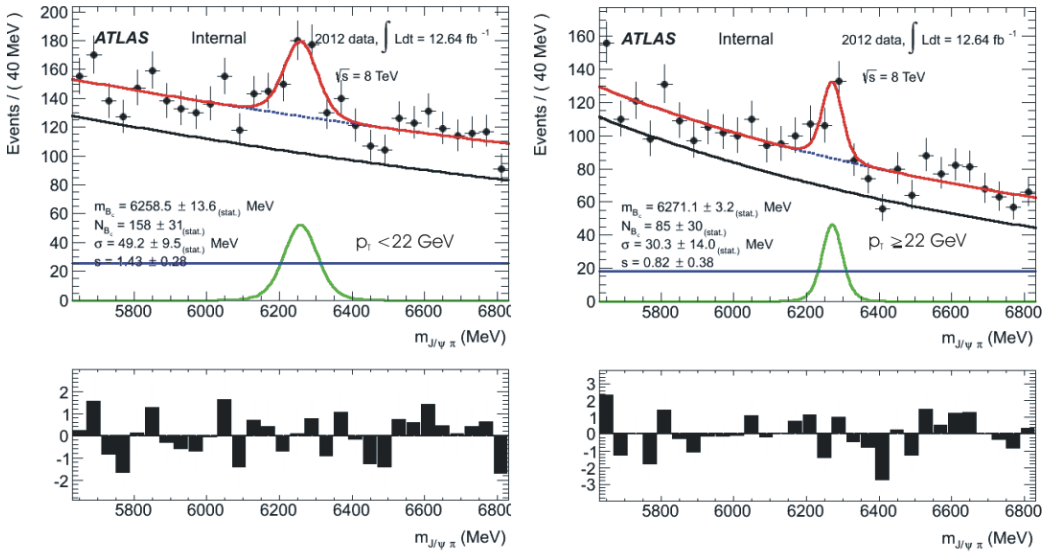

Figure 6.3: The fit of the invariant mass for the $B_c^{\pm}$ meson. The fit for the low transverse momentum bin ($13\,\text{GeV} < p_{\text{T}}(B_c^{\pm}) < 22\,\text{GeV}$) is shown on the left, and that for the high transverse momentum bin ($p_{\text{T}}(B_c^{\pm}) \geq 22\,\text{GeV}$) on the right. The fits are used to extract $N^{\text{reco}}(B_c^{+}) + N^{\text{reco}}(B_c^{-})$ and its uncertainty in each bin. The pull plots below the fits show the deviation of data from the fit in units of standard deviations.

The fits of the $B^{\pm}$ mass are shown in Figure 6.2. The data from 2012 data taking periods D, E, L are excluded from the fit, because they have been used in the study of the selection criteria. The numbers of events without efficiency correction in the remaining $12.64\,\text{fb}^{-1}$ of $\sqrt{s} = 8\,\text{TeV}$ data, in the two bins are

$$p_{\text{T}}(B^{\pm}) < 22\,\text{GeV}: \qquad N^{\text{reco}}(B^{+}) + N^{\text{reco}}(B^{-}) = 35\,792 \pm 214, \tag{6.12}$$

$$p_{\text{T}}(B^{\pm}) \geq 22\,\text{GeV}: \qquad N^{\text{reco}}(B^{+}) + N^{\text{reco}}(B^{-}) = 52\,210 \pm 261. \tag{6.13}$$

The uncertainties are statistical, returned from the fitting procedure. Systematic uncertainty due to the choice of fit model and the mass range for the fit will be discussed in Section 6.3. The fits of the $B_c^{\pm}$ mass are shown in Figure 6.3. The numbers of $B_c^{\pm}$ events without efficiency correction in the two p_{T} bins are

$$p_{\text{T}}(B_c^{\pm}) < 22\,\text{GeV}: \qquad N^{\text{reco}}(B_c^{+}) + N^{\text{reco}}(B_c^{-}) = 158 \pm 31, \tag{6.14}$$

$$p_{\text{T}}(B_c^{\pm}) \geq 22\,\text{GeV}: \qquad N^{\text{reco}}(B_c^{+}) + N^{\text{reco}}(B_c^{-}) = 85 \pm 30. \tag{6.15}$$

6.2 Efficiencies

In order to calculate (6.4) from these results, the reconstruction efficiencies $\epsilon(B^+)$, $\epsilon(B^-)$, $\epsilon(B_c^+)$, $\epsilon(B_c^-)$ and the kinematic acceptances $A(B^\pm)$ and $A(B_c^\pm)$ are required. The kinematic acceptances reflect the probability that the decay products of $B_c^\pm$ and $B^\pm$ fall into the fiducial volume of the detector. They are the major correction to the number of events[9]. The acceptances for the $B_c^\pm$ and the $B^\pm$ observed through their decay into a J/ψ and a hadron are expected to be identical and the ratio of the acceptances is $A(B^\pm)/A(B_c^\pm) = 1$. For this analysis only the calculation of the reconstruction efficiencies is required[27].

The efficiencies correct for incomplete detection due to detector effects and the selection criteria. They are different for the two $B^\pm$ charge states, because the K^- interact more with the detector material[9]. This difference between the charge states is measured at $\sqrt{s} = 7\,\text{TeV}$ to be $< 5\,\%$[9]. It is expected to be similar at $\sqrt{s} = 8\,\text{TeV}$. The charge asymetry is due to the different available combinations of quarks and anti-quarks in the kaon and pion. The antiquark $\bar{s}$ in the K^+ has fewer interaction channels with the detector nucleons than the quark s in the K^- and thus higher efficiency than the latter, because it is less likely to be absorbed before its detection is completed. For the $B_c^\pm$ the efficiency difference between the charge states is much smaller, since the pion valence includes only u, d quarks. The charge differences are neglected for this calculation, and the associated uncertainties are significantly smaller than other sources of uncertainty.

The efficiencies can be calculated based on Monte Carlo samples for the $B_c^\pm \to J/\psi\pi^\pm$ and the $B^\pm \to J/\psi K^\pm$ decays. For the $B_c^\pm \to J/\psi\pi^\pm$ decay they are given by the ratio of the number of reconstructed Monte Carlo events $N_{MC}^{\text{reco}}(B_c^\pm)$ after all cuts have been applied to the number of generated events $N_{MC}^{\text{gen}}(B_c^\pm)$ in the corresponding Monte Carlo sample:

$$\epsilon(B_c^\pm) = \left.\frac{N_{MC}^{\text{reco}}(B_c^\pm)}{N_{MC}^{\text{gen}}(B_c^\pm)}\right|_{p_\text{T}\text{ bin},\ \eta\in[-1.05;1.05]} . \tag{6.16}$$

The information on the number of generated events $N_{MC}^{\text{gen}}(B_c^\pm)$ are extracted from the Monte Carlo sample of the signal decay listed in Appendix A, Table A.

The calculation of the efficiencies for the $B^{\pm}$ is done analogously to (6.16). The Monte Carlo sample for the B^{+} signal decay is listed in Appendix A as well. In this sample only the decay of the B^{+} state was produced. It contains some B^{-} events, which are not taken into account in the counting as they are not decayed in the same way as the B^{+}. This analysis uses only the positve charge state for the $B_c^{\pm}$ and the $B^{\pm}$. The number $N_{MC}^{\mathrm{reco}}(B^{+})$ of the reconstructed B^{+} events shown in Table 6.2 contains a factor of 1.049 . This is an extrapolation to correct for the fact that the event-reconstruction was not successful for 4.9 % of the computation jobs.

For the calculation of the efficiencies the ratios of the total number of decays, $N_{MC}^{\mathrm{gen}}(B_c^{+})$ and $N_{MC}^{\mathrm{gen}}(B^{+})$, to the numbers of decays reconstructed after the detector simulation, the analysis procedure and application of the offline selection criteria including the mass range of the fitting procedure, $N_{MC}^{\mathrm{reco}}(B_c^{+})$ and $N_{MC}^{\mathrm{reco}}(B^{+})$, are used. They are shown in Table 6.1 for the B_c^{+} and in Table 6.2 for the B^{+}.

	$13\,\mathrm{GeV} < p_{\mathrm{T}} < 22\,\mathrm{GeV}$ bin	$p_{\mathrm{T}} \geq 22\,\mathrm{GeV}$ bin
Measurement efficiency	1.0 %	4.9 %
$N_{MC}^{\mathrm{reco}}(B_c^{+})$	411	606
$N_{MC}^{\mathrm{gen}}(B_c^{+})$	40 966	12 340

Table 6.1: The efficiencies $\epsilon(B_c^{+})$ of the measurement for the number of $B_c^{\pm} \to J/\psi\pi^{\pm}$ decays in the two p_{T} bins in the barrel region of the inner detector, and the number of generated and reconstructed events $N_{MC}^{\mathrm{gen}}(B_c^{+})$ and $N_{MC}^{\mathrm{reco}}(B_c^{+})$. The total number of generated B_c^{+} events $N_{MC}^{\mathrm{gen}}(B_c^{+})$ is 2 49 604.

	$13\,\mathrm{GeV} < p_{\mathrm{T}} < 22\,\mathrm{GeV}$ bin	$p_{\mathrm{T}} \geq 22\,\mathrm{GeV}$ bin
Measurement efficiency	1.26 %	6.67 %
$N_{MC}^{\mathrm{reco}}(B^{+})$	2 655	2 603
$N_{MC}^{\mathrm{gen}}(B^{+})$	210 449	38 992

Table 6.2: The efficiencies $\epsilon(B^{+})$ of the measurement for the number of $B^{\pm} \to J/\psi K^{\pm}$ decays in the two p_{T} bins in the barrel region of the inner detector, and the numbers of generated and reconstructed events, $N_{MC}^{\mathrm{gen}}(B^{+})$ and $N_{MC}^{\mathrm{reco}}(B^{+})$. The total number of generated B^{+} events $N_{MC}^{\mathrm{gen}}(B^{+})$ is 9 992 992.

The ratios of these values according to (6.16) are calculated in the barrel region for each bin in p_{T} separately. Bin-to-bin migration effects are included in the efficiency definition, as the $N_{MC}^{\mathrm{reco}}(B_c^+)$ and $N_{MC}^{\mathrm{reco}}(B^+)$ are not required to be generated in the p_{T} bin of their reconstruction. The into-bin and out-of-bin migration effects are included as well for the same reason: The $N_{MC}^{\mathrm{reco}}(B_c^+)$ and $N_{MC}^{\mathrm{reco}}(B^+)$ do not need to be generated in the pseudorapidity and p_{T} interval of their reconstruction. The difference seen between the efficiencies for the B^+ and the B_c^+ are mostly due to the use of the d_0-significance (Section 5) as selection criteria. The selection on the d_0-significance is sensitive to the lifetime of the particle. The lifetime of the B^+ ($(1.64 \pm 0.01)\,\mathrm{ps}$) is about three times longer than for the B_c^+[18; 15] ($(0.45 \pm 0.04)\,\mathrm{ps}$). Thus, the required minimum on the d_0-significance rejects more B_c^+ than B^+. Without this cut, the efficiency ratio is conform with the ratio of reconstruction efficiencies for the $J/\psi\pi^{\pm}$ to the $J/\psi K^{\pm}$ derived in [9] at $\sqrt{s} = 7\,\mathrm{TeV}$.

The overall number of generated and reconstructed events is obtained the same way as $N_{MC}^{\mathrm{gen}}(B^+)$ and $N_{MC}^{\mathrm{gen}}(B_c^+)$. It is needed for the discussion of the uncertainties on the efficiencies below (Section 6.3).

6.3 Uncertainties

The uncertainty $\Delta\left(f(x_1,\ldots,x_n)\right)$ on any function $f(x_1,\ldots,x_n)$ which depends of the variables $x_1, x_2, \ldots, x_n$ with the respective uncertainties $\Delta(x_1), \Delta(x_2), \ldots, \Delta(x_n)$ is calculated according to

$$\Delta\left(f(x_1,\ldots,x_n)\right) = \sqrt{\sum_{i=1}^{i=n}\left(\frac{\partial f(x_1,\ldots,x_n)}{\partial x_i}\cdot\Delta(x_i)\right)^2}, \tag{6.17}$$

where for $x_1, x_2, \ldots, x_n$ the measurement values are used. The systematic uncertainties cover uncertainties on the efficiencies and on the fitting procedure.

The efficiencies can be factorized into the product of the efficiency of the J/ψ-trigger $\epsilon^{\mathrm{trigger}}$, the efficiency of the muon spectrometer ϵ^{MS}, the efficiency of the inner detector ϵ^{ID}, and the efficiency of fitting the muons and the hadron to a common decay vertex $\epsilon^{\mathrm{vertex}}$[34]:

$$\epsilon = \epsilon^{\mathrm{trigger}}\cdot\epsilon^{\mathrm{MS}}(\mu^+)\cdot\epsilon^{\mathrm{MS}}(\mu^-)\cdot\left(\epsilon^{\mathrm{ID}}(\mu^{\pm})\right)^2\cdot\epsilon^{\mathrm{ID}}(X)\cdot\epsilon^{\mathrm{vertex}}, \tag{6.18}$$

where X is the K^+ for the efficiency of the B^+ and X is the π^+ for the efficiency of the B_c^+. The efficiencies for reconstructing μ^+ and μ^- can differ, because the toroidal magnetic field bends low p_T μ^+ tracks to higher pseudorapidities while μ^- are bent to lower pseudorapidities. The J/ψ, $\mu^\pm$ coming from the $B_c^\pm \to J/\psi\pi^\pm$ and the $B^\pm \to J/\psi K^\pm$ decay only differ slightly in their kinematic properties. The efficiencies $\epsilon^\mathrm{trigger}$, ϵ^MS, $\epsilon^\mathrm{ID}(\mu^\pm)$, and ϵ^vertex are thus almost identical between the $B_c^\pm$ and the $B^\pm$. The systematic uncertainty on the efficiency ratios is then primarily given by the systematic uncertainties on $\epsilon^\mathrm{ID}(X)$. It is dominated by the material description in the simulation of the detector[47]. The material density affects the K^+ and the π^+ detection in the same way.

The remaining uncertainty on the efficiencies consists of the uncertainty due to the limited size of the Monte Carlo sample, and systematic uncertainties in the event counting. The latter is estimated by $\pm\,2\,\%$.

The efficiencies obey Bernoulli statistics, because each event has the same probability to fulfill the different criteria imposed by the analysis and thus be counted or rejected. The uncertainty due to the limited size of the Monte Carlo sample is calculated as the square root of the variance

$$\sigma^2(k) = \frac{k}{N}\left(1 - \frac{k}{N}\right) \cdot N, \tag{6.19}$$

according to Bernoulli statistics.[1]

The k is the number of events passing the criteria and N is the number of events before these criteria have been applied. Equation (6.19) is used to calculate the uncertainty $\Delta(N_{MC}^\mathrm{gen})$ on the number of events from the Monte Carlo generation falling into the barrel region and the p_T bins. Equation (6.19) is also used for the calculation of the uncertainty $\Delta(N_{MC}^\mathrm{reco})$ on the reconstruction of these generated events, in which k/N is given by the efficiency ϵ. The contributions are added in quadrature according to (6.17) for each bin in p_T separately.

The uncertainties on the efficiencies for the B_c^+ measurement are given by

$$p_\mathrm{T}(B_c^\pm) < 22\,\mathrm{GeV}: \qquad \Delta\left(\epsilon(B_c^+)\right) = 0.05 \cdot 10^{-2}, \tag{6.20}$$

$$p_\mathrm{T}(B_c^\pm) \geq 22\,\mathrm{GeV}: \qquad \Delta\left(\epsilon(B_c^+)\right) = 0.2 \cdot 10^{-2}. \tag{6.21}$$

[1] This model breaks down when N_{MC}^reco approaches N_{MC}^gen or one of them gets close to zero, because errors would extend into unphysical regions [48; 49].

The uncertainties on the efficiencies for the B^+ are:

$$p_{\mathrm{T}}(B^{\pm}) < 22\,\mathrm{GeV}: \qquad \Delta\left(\epsilon(B^+)\right) = 0.035 \cdot 10^{-2}, \tag{6.22}$$

$$p_{\mathrm{T}}(B^{\pm}) \geq 22\,\mathrm{GeV}: \qquad \Delta\left(\epsilon(B^+)\right) = 0.2 \cdot 10^{-2}. \tag{6.23}$$

The uncertainties on the fitting procedure involve the choice of the signal model, the choice of the background model, and the choice of the mass range. They are estimated by fitting the invariant masses of the $B_c^{\pm}$ and the $B^{\pm}$ using alternative models for the signal and the background as described below. These fits are shown in Figure 6.4 and Figure 6.5 for the $B_c^{\pm}$ and in Figure 6.6, Figure 6.7, Figure 6.8, and Figure 6.9 for the $B^{\pm}$. The sources of uncertainty are treated as uncorrelated. The maximum deviations from $N^{\mathrm{reco}}(B_c^+) + N^{\mathrm{reco}}(B_c^-)$ and $N^{\mathrm{reco}}(B^+) + N^{\mathrm{reco}}(B^-)$ for each of the sources are added in quadrature according to (6.17) to form the systematic uncertainty on the fitted number of events.

The $B_c^{\pm}$ mass is fitted with a multi-Gaussian function as the signal model (6.6) and with an exponential function plus constant contribution for the background (6.8). In order to estimate the systematic uncertainties due to the fitting procedure, one of these contributions at a time is replaced by another function. The choice of the functions is the same as in the measurement by CMS at $\sqrt{s} = 7\,\mathrm{TeV}$[27]. The signal model is replaced by a Crystal Ball function

$$\mathcal{F}^{\mathrm{CB}}_{signal}(m_{J/\psi\pi^{\pm}}) \propto \begin{cases} \exp\left[-(m_{J/\psi\pi^{\pm}} - M_{B_c^{\pm}})^2/(2\sigma^2_{CB})\right], & \text{for } m_{J/\psi\pi^{\pm}} > M_{B_c^{\pm}} - \alpha\sigma_{CB}\,. \\ \frac{(n/\alpha)^n \exp(-\alpha^2/2)}{\left[(M_{B_c^{\pm}} - m_{J/\psi\pi^{\pm}})/\sigma_{CB} + n/\alpha - \alpha\right]^n}, & \text{for } m_{J/\psi\pi^{\pm}} \leq M_{B_c^{\pm}} - \alpha\sigma_{CB} \end{cases} \tag{6.24}$$

It describes a Gaussian signal peak of width σ_{CB} combined with a power law tail whose position depends on the value of α. The parameter n characterizes the length of this tail. This leads to an uncertainty of 1.9 % on $N^{\mathrm{reco}}(B_c^+) + N^{\mathrm{reco}}(B_c^-)$ for $p_{\mathrm{T}}(B_c^{\pm}) < 22\,\mathrm{GeV}$ and 7 % for $p_{\mathrm{T}}(B_c^{\pm}) \geq 22\,\mathrm{GeV}$.

The uncertainty on the choice of the background model is estimated by the maximum deviation from the signal yield $N^{\mathrm{reco}}(B_c^+) + N^{\mathrm{reco}}(B_c^-)$ for polynomial functions of first to third order. The maximum deviation is produced by a polynomial of first order. It results in an uncertainty estimation of 3.8 % for $p_{\mathrm{T}}(B_c^{\pm}) < 22\,\mathrm{GeV}$ and 21 % for $p_{\mathrm{T}}(B_c^{\pm}) \geq 22\,\mathrm{GeV}$.

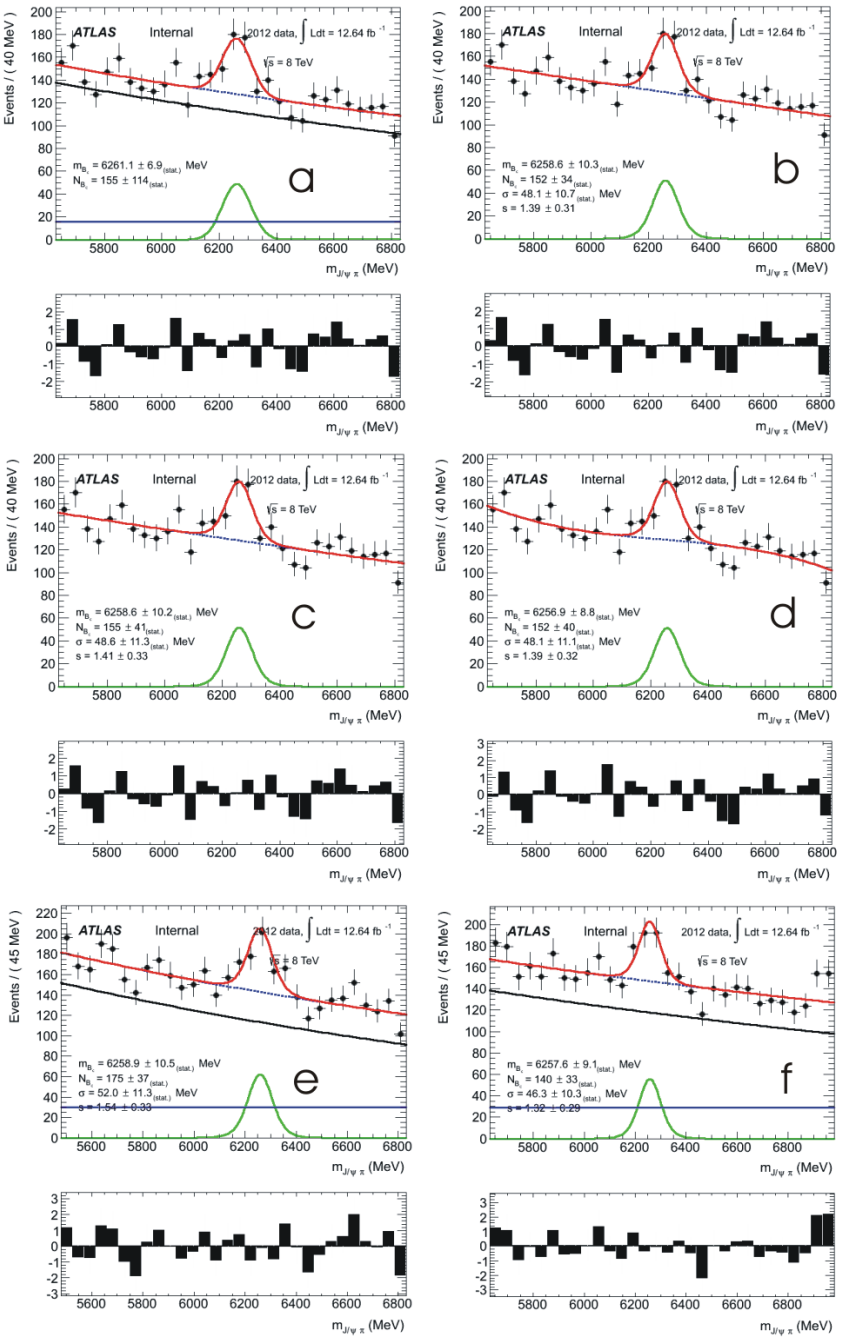

Figure 6.4: The influence of the signal model, background model, and mass range on the $B_c^{\pm}$ mass fit for $p_{\mathrm{T}} < 22\,\mathrm{GeV}$. The signal model is replaced by a Crystal Ball function (a). The background is modeled with first (b), second (c), and third order (d) polynomial functions. The mass range is varied to $5480\,\mathrm{MeV} < m^i_{J/\psi\pi^{\pm}} < 6830\,\mathrm{MeV}$ (e) and $5630\,\mathrm{MeV} < m^i_{J/\psi\pi^{\pm}} < 6980\,\mathrm{MeV}$ (f). The pull plots show the deviation of the fit from the data in units of standard deviations.

Signal model	Background model	Mass range	Deviation
Std.	1. order Polynomial	Std.	**6**
Std.	2. order Polynomial	Std.	3
Std.	3. order Polynomial	Std.	**6**
Std.	Std.	5.48 GeV ... 6.83 GeV	17
Std.	Std.	5.63 GeV ... 6.98 GeV	**18**
Crystal Ball	Std.	Std.	**3**

Table 6.3: The systematic uncertainty on the $B_c^\pm$ invariant mass fit for $p_\mathrm{T}(B_c^\pm) < 22\,\mathrm{GeV}$ in the barrel region of the detector. The standard signal model (6.6), background model (6.8) and mass range are abbreviated with Std. The modifications and the deviation from the number of decays observed with the standard $B_c^\pm$ fit are shown. The maximum deviation is highlighted in bold.

The uncertainty based on the choice of the mass range is estimated by varying the upper and lower limits by a few standard deviations. For both bins the upper bound is increased by 150 MeV. In a separate fit, the lower bound is decreased by 150 MeV. The maximum deviation is an estimate for the corresponding uncertainty. It leads to an uncertainty of 11 % for $p_\mathrm{T}(B_c^\pm) < 22\,\mathrm{GeV}$ and 9.4 % for $p_\mathrm{T}(B_c^\pm) \geq 22\,\mathrm{GeV}$.

The contributions to the systematic uncertainty on the $B_c^\pm$ fit are listed in Table 6.3 for $p_\mathrm{T}(B_c^\pm) < 22\,\mathrm{GeV}$ and Table 6.4 for $p_\mathrm{T}(B_c^\pm) \geq 22\,\mathrm{GeV}$. The systematic uncertainties due to the fit are thus

$$p_\mathrm{T}(B_c^\pm) < 22\,\mathrm{GeV}: \qquad \Delta\left(N^\mathrm{reco}(B_c^+) + N^\mathrm{reco}(B_c^-)\right)_\mathrm{fit} = 19, \tag{6.25}$$

$$p_\mathrm{T}(B_c^\pm) \geq 22\,\mathrm{GeV}: \qquad \Delta\left(N^\mathrm{reco}(B_c^+) + N^\mathrm{reco}(B_c^-)\right)_\mathrm{fit} = 21. \tag{6.26}$$

The systematic uncertainty from the fit model of the $B^\pm$ is estimated analogously to those of the $B_c^\pm$. It is slightly more complex, because the $B^\pm$ background model is a superposition of three different components. The functions used to estimate the uncertainties are the same as in the cross section measurement of the B^+ at $\sqrt{s} = 7\,\mathrm{TeV}$ by ATLAS[9]. The systematic uncertainty due to the choice of the mass range is studied, since it was observed to be an important contribution in the systematic uncertainty on the $B_c^\pm$ fit. The fits are shown in Figure 6.6 and Figure 6.7 for $p_\mathrm{T}(B^\pm) < 22\,\mathrm{GeV}$ and in Figure 6.8 and Figure 6.9 for $p_\mathrm{T}(B^\pm) \geq 22\,\mathrm{GeV}$.

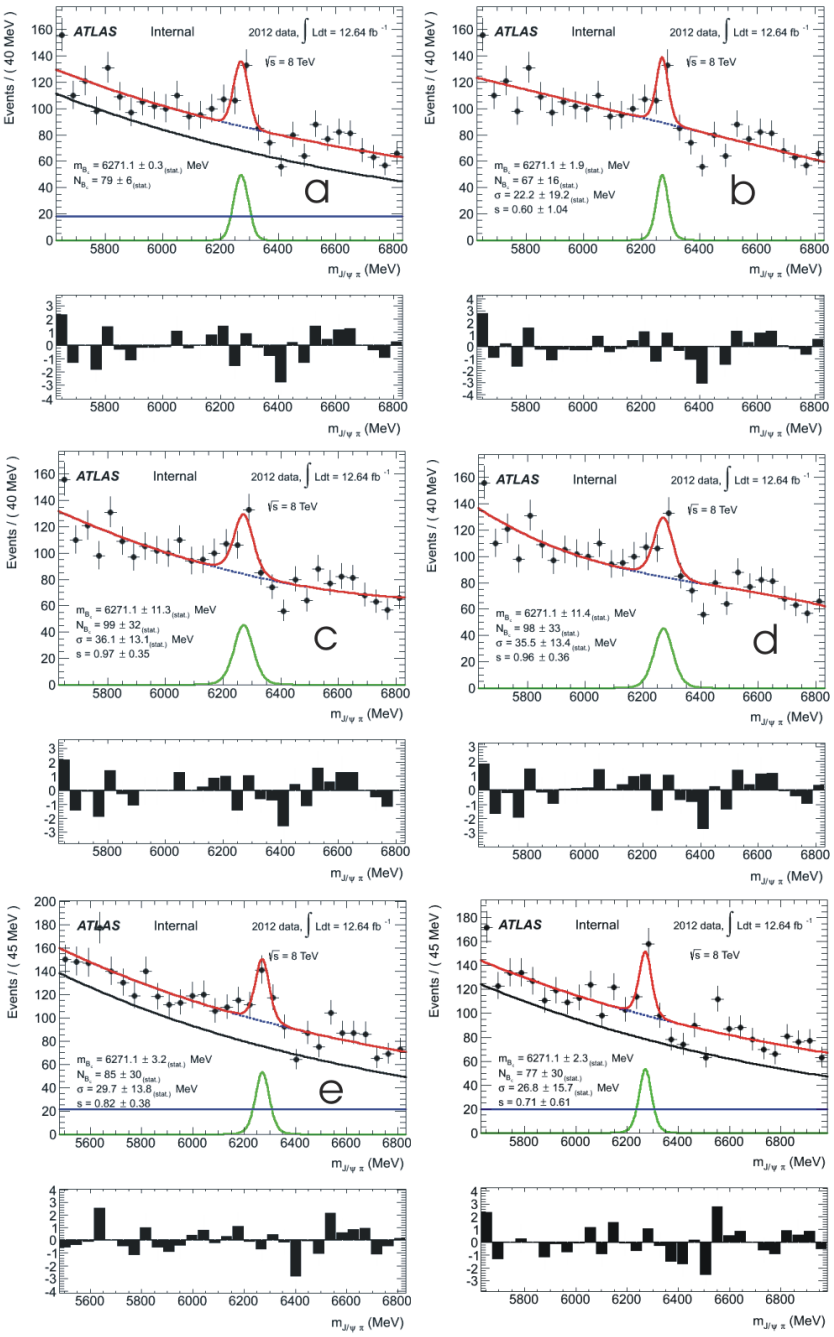

Figure 6.5: The influence of the signal model, background model and mass range on the $B_c^{\pm}$ mass fit for $p_{\mathrm{T}} \geq 22\,\mathrm{GeV}$. The signal model is replaced by a Crystal Ball function (a). The background is modeled with first (b), second (c), and third order (d) polynomial functions. The mass range is varied to $5480\,\mathrm{MeV} < m^i_{J/\psi\pi^{\pm}} < 6830\,\mathrm{MeV}$ (e) and $5630\,\mathrm{MeV} < m^i_{J/\psi\pi^{\pm}} < 6980\,\mathrm{MeV}$ (f). The pull plots show the deviation of the fit from the data in units of standard deviations.

Signal model	Background model	Mass range	Deviation
Std.	1. order Polynomial	Std.	**18**
Std.	2. order Polynomial	Std.	14
Std.	3. order Polynomial	Std.	13
Std.	Std.	5.48 GeV ... 6.83 GeV	0
Std.	Std.	5.63 GeV ... 6.98 GeV	**8**
Crystal Ball	Std.	Std.	**6**

Table 6.4: The systematic uncertainty on the $B_c^{\pm}$ invariant mass fit for $p_{\mathrm{T}}(B_c^{\pm}) \geq 22\,\mathrm{GeV}$ in the barrel region of the detector. The standard signal model (6.6), background model (6.8) and mass range are abbreviated with Std. The modifications and the deviation from the number of decays observed with the standard $B_c^{\pm}$ fit are shown. The maximum deviation is highlighted in bold.

To quantify uncertainty due to the choice of background model, the decaying exponential function (6.9) is replaced by polynomial functions of first to third order. In another fit the multi-Gaussian function modeling the Cabibbo-suppressed background (6.11) is replaced by a Crystal Ball function. The polynomial of second order produces the maximal deviation from $N^{\mathrm{reco}}(B^+) + N^{\mathrm{reco}}(B^-)$, resulting in a systematic uncertainty on the choice of the background model of 0.4 % for $p_{\mathrm{T}}(B^{\pm}) < 22\,\mathrm{GeV}$ and 0.3 % for $p_{\mathrm{T}}(B^{\pm}) \geq 22\,\mathrm{GeV}$. The complementary error function (6.10) is not modified. It is the best choice to model the mass distribution of the partially reconstructed states.

At low values of $m^i_{J/\psi K^{\pm}}$ the contribution of partially reconstructed states decreases, while the complementary error function is nearly constant. This is the reason why the lower mass limit can be only slightly manipulated. For the study of the influence of the mass range it is modified by $-50\,\mathrm{MeV}$. The upper limit of the mass range is increased by 200 MeV. The maximum deviation from $N^{\mathrm{reco}}(B^+) + N^{\mathrm{reco}}(B^-)$ is observed to be 1.7 % for $p_{\mathrm{T}}(B^{\pm}) < 22\,\mathrm{GeV}$ and 1.6 % for $p_{\mathrm{T}}(B^{\pm}) \geq 22\,\mathrm{GeV}$.

The uncertainty on the number of reconstructed $B^{\pm}$ events due to the choice of signal model is estimated in the same way as for the $B_c^{\pm}$. It is 0.04 % for $p_{\mathrm{T}}(B^{\pm}) < 22\,\mathrm{GeV}$ and 2.6 % for $p_{\mathrm{T}}(B^{\pm}) \geq 22\,\mathrm{GeV}$. Hence, it is the dominant contribution to the total systematic uncertainty on the $B^{\pm}$ fit models for the

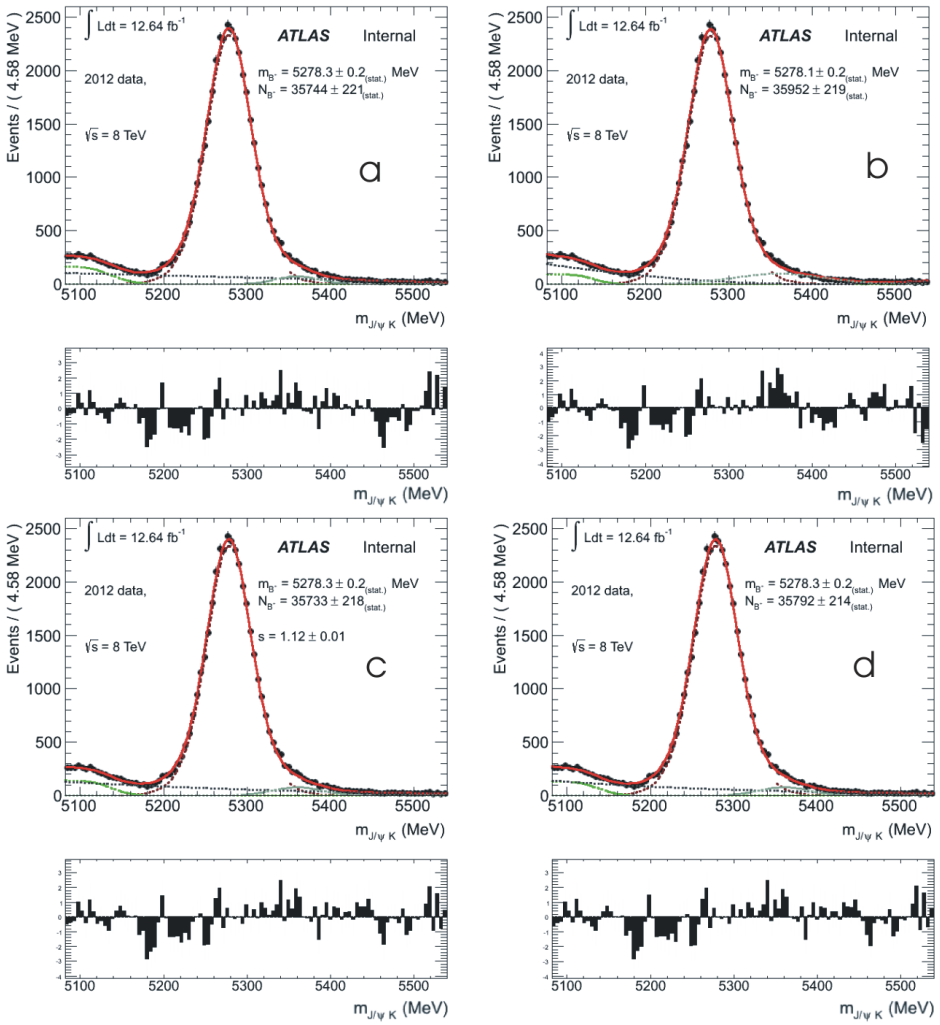

Figure 6.6: The influence of the background model on the $B^{\pm}$ mass fit for $p_{\mathrm{T}} < 22\,\mathrm{GeV}$. The combinatorial background is modeled with first (a), second (b), and third order (c) polynomial functions. The Cabibbo-suppressed background is modeled with a Crystal Ball function (d). The pull plots show the deviation of the fit from the data in units of the standard deviation.

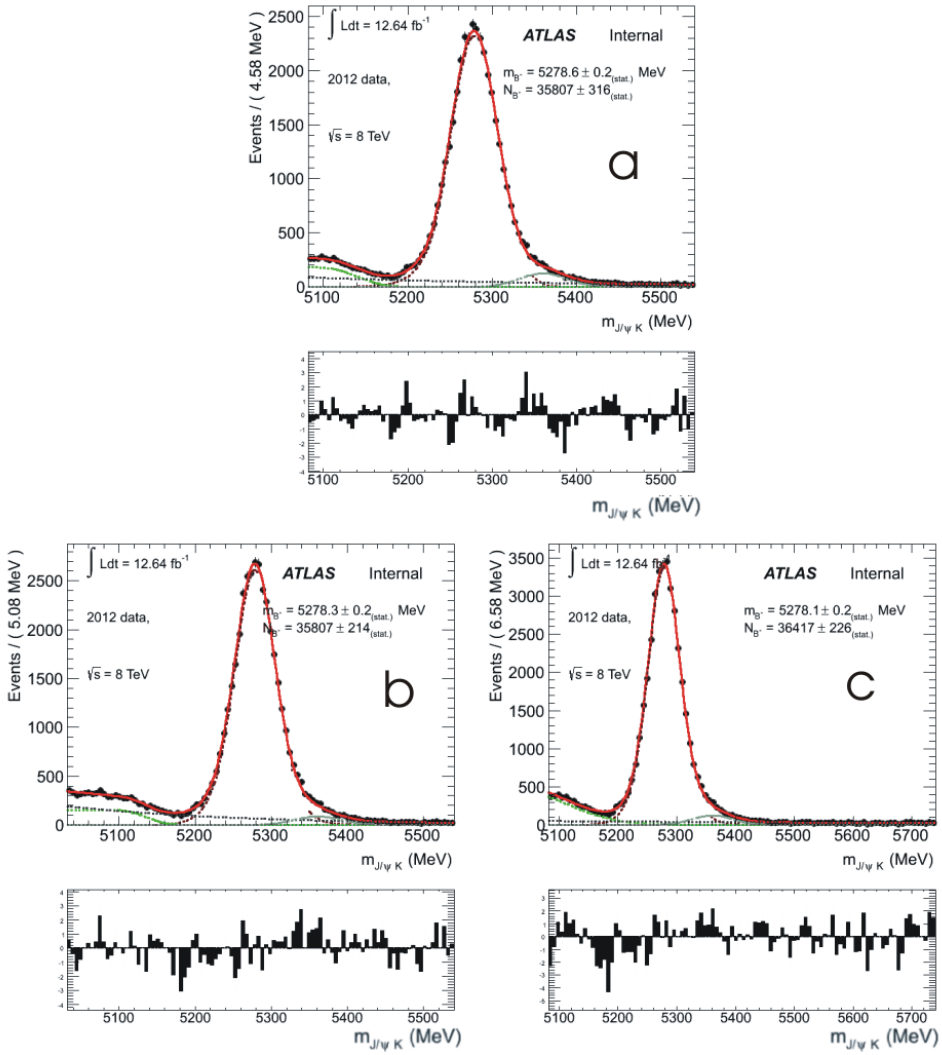

Figure 6.7: The influence of the signal model and the mass range on the $B^{\pm}$ mass fit for $p_{\mathrm{T}} < 22\,\mathrm{GeV}$. The signal model is replaced by a Crystal Ball function (a). The mass range is varied to $5032\,\mathrm{MeV} < m^{i}_{J/\psi K^{\pm}} < 5540\,\mathrm{MeV}$ (b) and $5082\,\mathrm{MeV} < m^{i}_{J/\psi K^{\pm}} < 5740\,\mathrm{MeV}$ (c). The pull plots show the deviation of the fit from the data in units of the standard deviation.

Signal model	Background model	Mass range	Deviation
Std.	Crystal Ball	Std.	0
Std.	1. order Polynomial	Std.	137
Std.	2. order Polynomial	Std.	**152**
Std.	3. order Polynomial	Std.	152
Std.	Std.	5.032 GeV . . . 5.54 GeV	37
Std.	Std.	5.082 GeV . . . 5.74 GeV	**851**
Crystal Ball	Std.	Std.	**1373**

Table 6.5: The systematic uncertainty on the $B^{\pm}$ invariant mass fit for $p_{\mathrm{T}}(B^{\pm}) \geq 22\,\mathrm{GeV}$ in the barrel region of the detector. The standard signal model (6.7), background models (6.9), (6.10), (6.11) and mass range are abbreviated with Std. The modifications and the deviation from the number of decays observed with the standard $B^{\pm}$ fit are shown. The maximum deviation is highlighted in bold.

Signal model	Background model	Mass range	Deviation
Std.	Crystal Ball	Std.	1
Std.	1. order Polynomial	Std.	48
Std.	2. order Polynomial	Std.	**160**
Std.	3. order Polynomial	Std.	59
Std.	Std.	5.032 GeV . . . 5.54 GeV	15
Std.	Std.	5.082 GeV . . . 5.74 GeV	**625**
Crystal Ball	Std.	Std.	**15**

Table 6.6: The systematic uncertainty on the $B^{\pm}$ invariant mass fit for $p_{\mathrm{T}}(B^{\pm}) < 22\,\mathrm{GeV}$ in the barrel region of the detector. The standard signal model (6.7), background models (6.9), (6.10), (6.11) and mass range are abbreviated with Std. The modifications and the deviation from the number of decays observed with the standard $B^{\pm}$ fit are shown. The maximum deviation is highlighted in bold.

high p_{T} bin. In the low p_{T} region, the systematic uncertainty of the fit is dominated by the uncertainty on the choice of mass region. The contributions to the systematic uncertainties on the $B^{\pm}$ fit are displayed in Table 6.6 for $p_{\mathrm{T}}(B^{\pm}) < 22\,\mathrm{GeV}$ and in Table 6.5 for $p_{\mathrm{T}}(B^{\pm}) \geq 22\,\mathrm{GeV}$. The total systematic uncertainty on the $B^{\pm}$ fit is calculated by adding the three contributions in quadrature, leading to:

$$p_{\mathrm{T}} < 22\,\mathrm{GeV}: \qquad \Delta\left(N^{\mathrm{reco}}(B^{+}) + N^{\mathrm{reco}}(B^{-})\right)_{\mathrm{fit}} = 645, \tag{6.27}$$

$$p_{\mathrm{T}} \geq 22\,\mathrm{GeV}: \qquad \Delta\left(N^{\mathrm{reco}}(B^{+}) + N^{\mathrm{reco}}(B^{-})\right)_{\mathrm{fit}} = 1\,622. \tag{6.28}$$

The systematic uncertainty on the $B_c^{\pm}$ fit (12 % for $p_{\mathrm{T}}(B_c^{\pm}) < 22\,\mathrm{GeV}$ and 25 % for $p_{\mathrm{T}}(B_c^{\pm}) \geq 22\,\mathrm{GeV}$) dominates over the uncertainty on the $B^{\pm}$ fit (3 %).

The systematic uncertainty on the relative measurement is calculated with the uncertainty results (6.25), (6.26), (6.27), (6.28) for the systematic uncertainties on the fits and (6.20), (6.21), (6.22), (6.23) for the uncertainties on the efficiencies using (6.17). This leads to the final uncertainties

$$p_{\mathrm{T}} < 22\,\mathrm{GeV}: \qquad \Delta\left(\frac{\sigma(B_c^{+}) \cdot BR(B_c^{+} \to J/\psi\pi^{+})}{\sigma(B^{+}) \cdot BR(B^{+} \to J/\psi K^{+})}\right)_{\mathrm{syst}} = 0.07 \cdot 10^{-2}, \tag{6.29}$$

$$p_{\mathrm{T}} \geq 22\,\mathrm{GeV}: \qquad \Delta\left(\frac{\sigma(B_c^{+}) \cdot BR(B_c^{+} \to J/\psi\pi^{+})}{\sigma(B^{+}) \cdot BR(B^{+} \to J/\psi K^{+})}\right)_{\mathrm{syst}} = 0.06 \cdot 10^{-2}. \tag{6.30}$$

The statistical uncertainty on the measurement can be calculated from the uncertainties on the fit to the invariant mass. They are given in (6.14) and (6.15) for the statistical uncertainties on the numbers of reconstructed $B_c^{\pm}$, $\Delta\left(N^{\mathrm{reco}}(B_c^{+}) + N^{\mathrm{reco}}(B_c^{-})\right)$. The statistical uncertainties on the numbers of reconstructed $B^{\pm}$ decays, $\Delta\left(N^{\mathrm{reco}}(B^{+}) + N^{\mathrm{reco}}(B^{-})\right)$, are given in (6.12) and (6.13). The statistical uncertainties on the measurements are calculated according to (6.17):

$$p_{\mathrm{T}} < 22\,\mathrm{GeV}: \qquad \Delta\left(\frac{\sigma(B_c^{\pm}) \cdot BR(B_c^{\pm} \to J/\psi\pi^{\pm})}{\sigma(B^{\pm}) \cdot BR(B^{\pm} \to J/\psi K^{\pm})}\right)_{\mathrm{stat}} = 0.1 \cdot 10^{-2}, \tag{6.31}$$

$$p_{\mathrm{T}} \geq 22\,\mathrm{GeV}: \qquad \Delta\left(\frac{\sigma(B_c^{\pm}) \cdot BR(B_c^{\pm} \to J/\psi\pi^{\pm})}{\sigma(B^{\pm}) \cdot BR(B^{\pm} \to J/\psi K^{\pm})}\right)_{\mathrm{stat}} = 0.08 \cdot 10^{-2}. \tag{6.32}$$

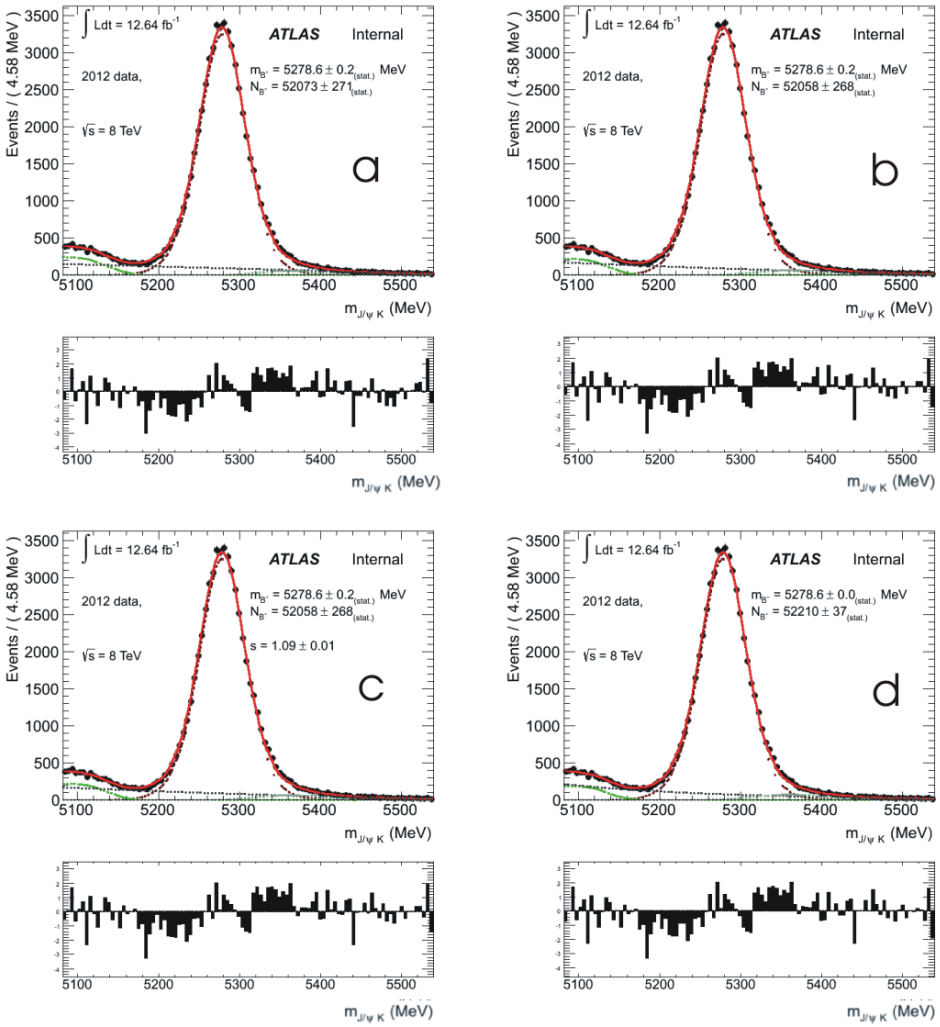

Figure 6.8: The influence of background model on the $B^{\pm}$ mass fit for $p_{\mathrm{T}} \geq 22\,\mathrm{GeV}$. The combinatorial background is modeled with first (a), second (b), and third order (c) polynomial functions. The Cabibbo suppressed background is modeled with a Crystal Ball function (d). The pull plots show the deviation of the fit from the data in units of the standard deviation.

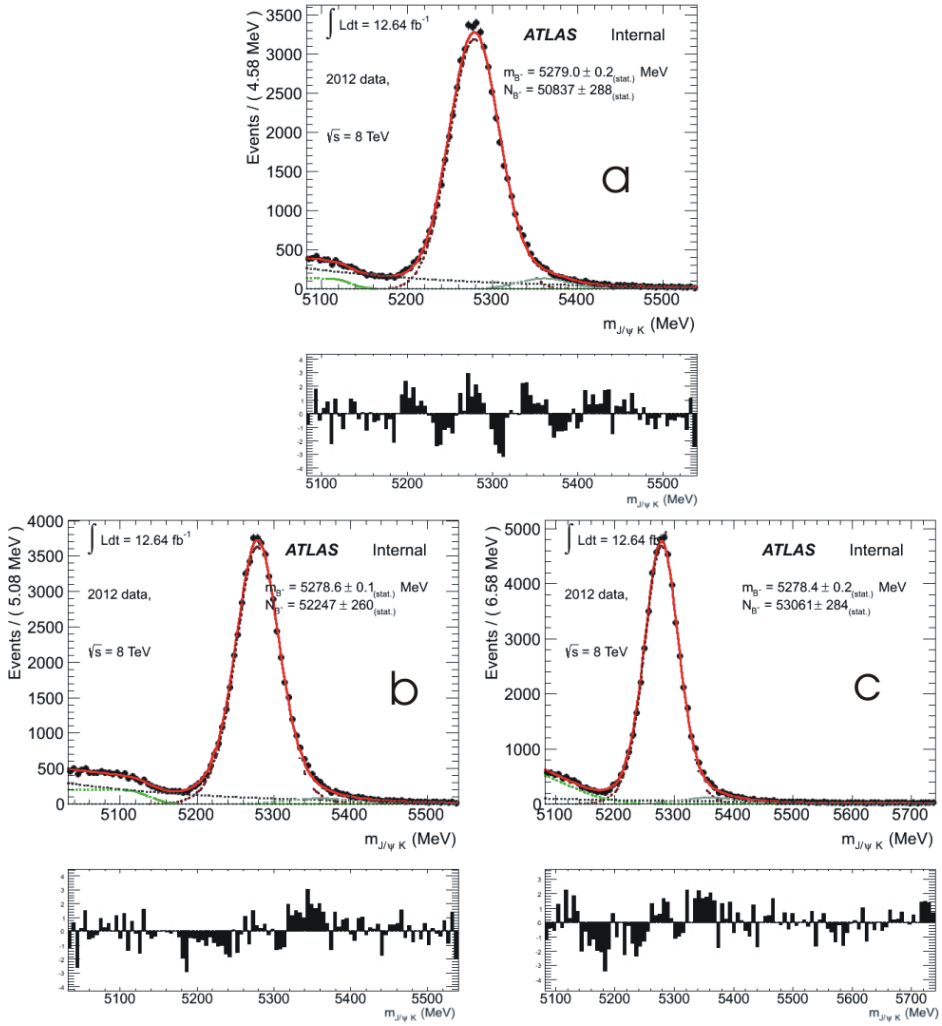

Figure 6.9: The influence of the signal model and the mass range on the $B^{\pm}$ mass fit for $p_{\mathrm{T}} < 22\,\mathrm{GeV}$. The signal model is replaced by a Crystal Ball function (a). The mass range is varied to $5032\,\mathrm{MeV} < m^{i}_{J/\psi K^{\pm}} < 5540\,\mathrm{MeV}$ (b) and $5082\,\mathrm{MeV} < m^{i}_{J/\psi K^{\pm}} < 5740\,\mathrm{MeV}$ (c). The pull plots show the deviation of the fit from the data in units of the standard deviation.

7 Results

With the yields (6.12), (6.13), (6.14), (6.15), the efficiencies from Table 6.1 and Table 6.2, the systematic uncertainties (6.29), (6.30), and the statistical uncertainties according to (6.31) and (6.32), the final result for this measurement of the production cross section of $B_c^\pm$ mesons observed through their decay to $J/\psi\pi^\pm$, relative to the production cross section of $B^\pm$ mesons observed through their decay to $J/\psi K^\pm$, using the ATLAS detector at $\sqrt{s} = 8\,\text{TeV}$, can be calculated for $|\eta| < 1.05$ using (6.4). The sum of the efficiencies for the two different charge states is replaced by the efficiencies for the B^+ and the B_c^+ respectively and the ratio of the acceptances is set to one. The calculation was performed for two bins in the transverse momentum p_T of the B meson ($B^\pm$ or $B_c^\pm$). The results are:

$13\,\text{GeV} < p_\text{T}(B_c^\pm), p_\text{T}(B^\pm) < 22\,\text{GeV}$:

$$\boxed{\frac{\frac{\mathrm{d}\sigma(B_c^\pm)}{\mathrm{d}p_\text{T}(B_c^\pm)} \cdot BR(B_c^\pm \to J/\psi\pi^\pm)}{\frac{\mathrm{d}\sigma(B^\pm)}{\mathrm{d}p_\text{T}(B^\pm)} \cdot BR(B^\pm \to J/\psi K^\pm)} = (0.56 \pm 0.11_\text{stat} \pm 0.07_\text{syst})\ \%,} \tag{7.1}$$

$p_\text{T}(B_c^\pm), p_\text{T}(B^\pm) \geq 22\,\text{GeV}$:

$$\boxed{\frac{\frac{\mathrm{d}\sigma(B_c^\pm)}{\mathrm{d}p_\text{T}(B_c^\pm)} \cdot BR(B_c^\pm \to J/\psi\pi^\pm)}{\frac{\mathrm{d}\sigma(B^\pm)}{\mathrm{d}p_\text{T}(B^\pm)} \cdot BR(B^\pm \to J/\psi K^\pm)} = (0.22 \pm 0.08_\text{stat} \pm 0.06_\text{syst})\ \%.} \tag{7.2}$$

The bins can also be combined to give the relative production cross section times branching fractions for $p_{\mathrm{T}} > 13\,\mathrm{GeV}$ and $|\eta| < 1.05$,

$$\frac{\sigma(B_c^{\pm}) \cdot BR(B_c^{\pm} \to J/\psi\pi^{\pm})}{\sigma(B^{\pm}) \cdot BR(B^{\pm} \to J/\psi K^{\pm})} = \frac{\left[\frac{\left(N^{\mathrm{reco}}(B_c^+)+N^{\mathrm{reco}}(B_c^-)\right)}{\left\langle\epsilon(B_c^{\pm})\right\rangle}\right]_{p_{\mathrm{T}}<22\,\mathrm{GeV}} + \left[\frac{\left(N^{\mathrm{reco}}(B_c^+)+N^{\mathrm{reco}}(B_c^-)\right)}{\left\langle\epsilon(B_c^{\pm})\right\rangle}\right]_{p_{\mathrm{T}}\geq 22\,\mathrm{GeV}}}{\left[\frac{(N^{\mathrm{reco}}(B^+)+N^{\mathrm{reco}}(B^-))}{\langle\epsilon(B^{\pm})\rangle}\right]_{p_{\mathrm{T}}<22\,\mathrm{GeV}} + \left[\frac{(N^{\mathrm{reco}}(B^+)+N^{\mathrm{reco}}(B^-))}{\langle\epsilon(B^{\pm})\rangle}\right]_{p_{\mathrm{T}}\geq 22\,\mathrm{GeV}}}. \tag{7.3}$$

The numerical value of (7.3) is

$p_{\mathrm{T}}(B_c^{\pm}), p_{\mathrm{T}}(B^{\pm}) > 13\,\mathrm{GeV}$:

$$\boxed{\frac{\sigma(B_c^{\pm}) \cdot BR(B_c^{\pm} \to J/\psi\pi^{\pm})}{\sigma(B^{\pm}) \cdot BR(B^{\pm} \to J/\psi K^{\pm})} = (0.48 \pm 0.09_{\mathrm{stat}} \pm 0.12_{\mathrm{syst}})\ \%}. \tag{7.4}$$

This result compares well to the measurement of the CMS Collaboration[27] at $\sqrt{s} = 7\,\mathrm{TeV}$. They have measured the relative production cross section times branching ratio in a similar fiducial region. Their measurement in the transverse region of $|y| < 1.6$ with $p_{\mathrm{T}}(B_c^{\pm}), p_{\mathrm{T}}(B^{\pm}) > 15\,\mathrm{GeV}$ was given by $\left(0.48 \pm 0.05_{\mathrm{stat}} \pm 0.04^{+0.05}_{\mathrm{syst}}{}_{-0.03_{\mathrm{lifetime}}}\right)$ %. A possible dependency on the center of mass energy $\sqrt{s}$ might be hidden by the uncertainties.

The measurement results for the two bins in p_{T} (7.1) and (7.2) show a dependency on the transverse momentum. The production cross section of the $B_c^{\pm}$ decreases faster with p_{T} than the production cross section of the $B^{\pm}$. B mesons with low transverse momentum will go into regions of higher pseudorapidity than those with high transverse momentum due to the conservation of momentum and energy. It can be expected that a measurement in the forward region would result in a higher production cross section ratio. The LHCb Collaboration has performed a measurement in the forward region[17], $2.5 < \eta < 4.5$, at $\sqrt{s} = 7\,\mathrm{TeV}$. Their result is $(0.68 \pm 0.10_{\mathrm{stat}} \pm 0.03_{\mathrm{syst}} \pm +0.05_{\mathrm{lifetime}})$ %. Within their uncertainties all three measurements are compatible.

8 Outlook

In this analysis the optimal selection criteria for the $B_c^\pm$ have been studied using a data based approach. The results allowed to significantly improve the $B_c^\pm$ yield by a factor of two compared to previous ATLAS analyses. This was crucial and made a calculation of the relative production cross section times branching ratio in two bins in p_T possible. The number of $B_c^\pm$ and $B^\pm$ were obtained from a fit to the invariant mass distribution and corrected for the detection efficiencies. It could be shown that the decrease in the production cross section with increasing transverse momentum is stronger for the $B_c^\pm$ than for the $B^\pm$ in the transverse region.

This is the first measurement of the production cross section for the $B_c^\pm$ times branching fraction to $J/\psi\pi^\pm$ relative to the $B^\pm$ production cross section times branching fraction to $J/\psi K^\pm$ with the ATLAS detector and the first measurement with a center of mass energy of $\sqrt{s} = 8\,\mathrm{TeV}$. It prepares the way for a measurement of the absolute production cross section times branching ratio $\sigma(B_c^\pm) \cdot BR(B_c^\pm \to J/\psi\pi^\pm) \cdot BR(J/\psi \to \mu^+\mu^-)$. For that measurement the calculation of the acceptance and an accurate measurement of the integrated luminosity are important. The absolute production cross section could be measured directly from (2.5) using (6.2).

A better way of calculating the total production cross section for the $B_c^\pm$ would be to measure the total $B^\pm$ cross section at $\sqrt{s} = 8\,\mathrm{TeV}$ in the same p_T and $|\eta|$ regions and multiply the results (7.1), (7.2), (7.4) with these number. This will lead to a more precise absolute $B_c^\pm$ cross section result, because the $B^\pm$ cross section can be calculated with high accuracy due to higher statistics than for the $B_c^\pm$. With the help of the $B^\pm$ cross section for a similar fiducial volume $|y| < 1.0$ measured at $\sqrt{s} = 7\,\mathrm{TeV}$[9], the expectation values for the total $B_c^\pm$ production cross section averages can be estimated. The total $B_c^\pm$ production cross section times branching ratio averaged over the $13\,\mathrm{GeV} < p_\mathrm{T}(B_c^\pm) < 22\,\mathrm{GeV}$ bin is

expected to be

$$\left\langle \sigma(B_c^{\pm}) \right\rangle_{p_{\mathrm{T}}(B_c^{\pm})<22\,\mathrm{GeV}} \cdot BR(B_c^{\pm} \to J/\psi\pi^{\pm}) \cdot BR(J/\psi \to \mu^+\mu^-) \approx (0.25 \pm 0.07)\,\mathrm{pb},$$

and the total $B_c^{\pm}$ production cross section times branching ratio averaged over the $p_{\mathrm{T}}(B_c^{\pm}) \geq 22\,\mathrm{GeV}$ bin is expected to be

$$\left\langle \sigma(B_c^{\pm}) \right\rangle_{p_{\mathrm{T}}(B_c^{\pm})\geq 22\,\mathrm{GeV}} \cdot BR(B_c^{\pm} \to J/\psi\pi^{\pm}) \cdot BR(J/\psi \to \mu^+\mu^-) \approx (0.025 \pm 0.01)\,\mathrm{pb}.$$

The biggest contribution to the uncertainties on this measurement comes from the statistical and systematic uncertainties on the $B_c^{\pm}$ mass fits. A more detailed model of the background composition to the $B_c^{\pm}$ invariant mass shape could significantly increase the accuracy of such a measurement, but requires a better theoretical understanding of the background contributions. The precision of the measurement could strongly improve with higher $B_c^{\pm}$ statistics. With increased luminosity in LHC Run2, a relative and absolute cross section measurement at $\sqrt{s} = 13\,\mathrm{TeV}$ can be performed with higher accuracy. The results could be further strengthened by studying the influence of the detector description on the ratio of the efficiencies and studying different contributions to the efficiencies separately. A multi-parameter optimization procedure might lead to further improvements in the choice of the selection criteria.

This analysis focused on the barrel region of the detector, where ATLAS has its highest resolution. Additional studies of the relative production cross section over $1.05 < |\eta| < 2.5$ could lead to more insight into the spatial dependence of the fragmentation of heavy quarks. This is not within the scope of this thesis.

Appendix

A Data Sets

Monte Carlo samples

Channel	AMI Tag[1]
$B_c^+ \to J/\psi K^+$	mc12_8TeV.108602.PythiaBc_ Bc_JPsi_mu2p5mu2p5_K .merge.AOD.e1988_a188_a180_r3549
$B_c^+ \to J/\psi \rho^+$	mc12_8TeV.108603.PythiaBc_ Bc_JPsi_mu2p5mu2p5_Rho .merge.AOD.e1988_a188_a180_r3549
$B_c^+ \to J/\psi \nu \mu$	mc12_8TeV.108604.PythiaBc_ Bc_JPsi_mu2p5mu2p5_MuNu .merge.AOD.e1988_a188_a180_r3549
$B_c^+ \to J/\psi \pi^+ \pi^0$	mc12_8TeV.108605.PythiaBc_ Bc_JPsi_mu2p5mu2p5_2Pi .merge.AOD.e1988_a188_a180_r3549
$B_c^+ \to J/\psi \pi^+ \pi^+ \pi^-$	mc12_8TeV.108606.PythiaBc_ Bc_JPsi_mu2p5mu2p5_3Pi .merge.AOD.e1988_a188_a180_r3549
$b\bar{b} \to J/\psi X$	mc12_8TeV.208201.Pythia8B_ AU2_CTEQ6L1_bb_Jpsimu4mu4 .merge.AOD.e1454_a159_a180_r3549
$pp \to J/\psi X$	mc12_8TeV.208011.Pythia8B_ AU2_CTEQ6L1_pp_Jpsimu2p5mu2p5 .merge.AOD.e1623_a159_a180_r3549
$B_c^+ \to J/\psi \pi^+$	mc12_8TeV.108601.PythiaBc_ Bc_JPsi_mu2p5mu2p5_Pi .merge.AOD.e1988_a188_a180_r2549
$B^+ \to J/\psi K^+$	mc12_8TeV.208406.Pythia8B_AU2_ CTEQ6L1_Bplus_Jpsi_mu2p5mu2p5_Kplus .merge.AOD.e1998_a188_a180_r3549

Table A.1: The reconstruction requirements are applied to the official 2012 Monte Carlo data sets shown here. They are used to study the background composition. The AMI tag is given in this table. The signal $B_c^+ \to J/\psi \pi^+$ is used when optimizing the cuts. Together with the $B^+ \to J/\psi K^+$ sample it is also used for the calculation of the efficiencies.

Data sets

Period	AMI Tag
D	data12_8TeV.periodD.physics_Bphysics.PhysCont .DAOD_JPSIMUMU.grp14_v04_p1425
E	data12_8TeV.periodE.physics_Bphysics.PhysCont .DAOD_JPSIMUMU.grp14_v03_p1425
L	data12_8TeV.periodL.physics_Bphysics.PhysCont .DAOD_JPSIMUMU.grp14_v03_p1425
H	data12_8TeV.periodH.physics_Bphysics.PhysCont .DAOD_JPSIMUMU.grp14_v04_p1425
C	data12_8TeV.periodC.physics_Bphysics.PhysCont .DAOD_JPSIMUMU.grp14_v04_p1425
J	data12_8TeV.periodJ.physics_Bphysics.PhysCont .DAOD_JPSIMUMU.grp14_v03_p1425
B	data12_8TeV.periodB.physics_Bphysics.PhysCont .DAOD_JPSIMUMU.grp14_v03_p1425
G	data12_8TeV.periodG.physics_Bphysics.PhysCont .DAOD_JPSIMUMU.grp14_v03_p1425
I	data12_8TeV.periodI.physics_Bphysics.PhysCont .DAOD_JPSIMUMU.grp14_v03_p1425

Table A.2: The sets of 2012 data with $\sqrt{s} = 8\,\text{TeV}$. The reconstruction requirements are applied to these data sets (5.4), but with a cut of $p_{\text{T}}(\pi^+) > 3\,\text{GeV}$. Periods D, E, and L are excluded in the data analysis. They are used with a reconstruction criterion of $p_{\text{T}}(\pi^+) > 500\,\text{MeV}$ for the study of the selection criteria.

B Lists

B.1 List of Figures

B.2 List of Tables

C Bibliography

[1] ATLAS Collaboration, "Observation of a new particle in the search for the Standard Model Higgs boson with the ATLAS detector at the LHC," Phys. Lett., **B 716** 1 (2012), arXiv:1207.7214[hep-ex].

[2] CMS Collaboration, "Observation of a new boson at a mass of 125 GeV with the CMS experiment at the LHC," Phys. Lett., **B 716** 30 (2012), arXiv:1207.7235.

[3] L. Evans, P. Bryant (editors), "LHC Machine," JINST, **3** S08001 (2008).

[4] CDF Collaboration, "Observation of the B_c meson in $p\bar{p}$ collisions at $\sqrt{s} = 1.8$ TeV," Phys. Rev. Lett., **81** 2432 (1998), arXiv:hep-ex/9805034.

[5] ATLAS Collaboration, "Observation of the $B_c^{\pm}$ meson in the decay $B_c^{\pm} \to J/\psi(\mu^+\mu^-)\pi^{\pm}$ with the ATLAS detector at the LHC," ATLAS-CONF-2012-028 (2012).

[6] A.V. Berezhnoy, A.K. Likhoded, M.V. Shelyagin, "Hadronic production of B_c mesons," Phys. Atom. Nucl., **58** 672 (1995), arXiv:hep-ph/9408284.

[7] J. Collins, D. Soper, G. Sterman, "Factorization of Hard Processes in QCD," Adv. Ser. Direct, High Energy Phys., **5** 1 (1998), arXiv:hep-ph/0409313[hep-ph].

[8] C.H. Chang, Y.Q. Chen, G.P. Han, H.T. Jiang, "On Hadronic Production ot the B_c Meson," Phys. Rev. D, **48** 4086 (1993), arXiv:hep-ph/9408242.

[9] I. Nomidis, "Study of the b-quark properties with the first ATLAS data," Ph.D. thesis, Arisotle University of Thessaloniki (2013), CERN-THESIS-2013-261.

[10] R.K. Ellis, W.J. Stirling, B.R. Webber, "QCD and Collider Physics," Cambridge Monographs on Particle Physics, Nuclear Physics and Cosmology, 193 (1996).

[11] E. Ben-Haim, "The b Quark Fragmentation Function, From LEP to TeVatron," Ph.D. thesis, Université Pierre & Marie Curie, Paris 6 (2004).

[12] M. Kobayashi, T. Maskawa, "CP-Violation in the Renormalizable Theory of Weak Interaction," Progress of Theoretical Physics, **49(2)** 652 (1973).

[13] S. Fiorendi, "Study of the $B_c \to J/\psi\pi$ and $B \to J/\psi K$ decay channels in the CMS experiment at LHC," Ph.D. thesis, Università degli studi di Milano (2011).

[14] V. V. Kiselev, S. S. Gershtein, et al., "Theoretical status of the B_c meson," IFVE-98-22, IHEP-98-22 (1998).

[15] J. Beringer (Particle Data Group), et al., "Bottom, Charmed Mesons," PRD, **86** 010001 (2012), http://pdg.lbl.gov/2011/tables/rpp2011-tab-mesons-bottom-charm.pdf.

[16] CDF Collaboration, "Evidence for the exclusive decay $B_c^{\pm} \to J/\psi\pi^{\pm}$ and measurement of the mass of the $B_c^{\pm}$ meson," Phys. Rev. Lett., **96** 82002 (2006), arXiv:hep-ex/0505076v3.

[17] LHCb Collaboration, "Measurements of B_c^+ production and mass with the $B_c^+ \to J/\psi\pi^+$ decay," Phys. Rev. Lett., **109** 232001 (2012), arXiv:1209.5634.

[18] K. Nakamura (Particle Data Group), et al., "table: bottom mesons," JP G, **37** 75021 (2010), http://pdg.lbl.gov/2011/tables/rpp2011-tab-mesons-bottom.pdf.

[19] J. Butler, R. Leroy (editor), "B Physics at Hadron Colliders," Rev. Sci. Instrum., **77** 525 (2006), FERMILAB-PUB-05-623-E.

[20] ATLAS Collaboration, "The ATLAS Experiment at the CERN Large Hadron Collider," JINST, **3** S08003 (2008).

[21] K. Assamagan, et al., *Computing Workbook*, ATLAS-twiki: https://twiki.cern.ch/twiki/bin/view/AtlasComputing/WorkBook (August 2013).

[22] ATLAS Collaboration, "Preliminary results on the muon reconstruction efficiency, momentum resolution, and momentum scale in ATLAS 2012 pp collision data," ATLAS-CONF-2013-088 (2013).

[23] B. Gorini, et al. (editors), *The ATLAS Data Acquisition and High-Level Trigger: Concept, Design and Status*, http://indico.cern.ch/event/048/contributions (2006).

[24] CDF Collaboration, "Measurement of the Branching Fraction $B(B_u^+ \to J/\psi\pi^+)$ and Search for $B_c^+ \to J/\psi\pi^+$," Phys. Rev. Lett. **77**, 5176 (1996).

[25] R. Aaij, et al., "First Observation of the Decay $B_c^+ \to J/\psi\pi^+\pi^-\pi^+$," Phys. Rev. Lett., **108** 251802 (2012).

[26] CMS Collaboration, "Observation of the decays $B_c^+ \to J/\psi\pi^+$ and $B_c^+ \to J/\psi\pi^+\pi^+\pi^-$ in pp collisions at $\sqrt{s} = 7\,\text{TeV}$," CMS PAS BPH-11-003 (2012).

[27] CMS Collaboration, "Measurement of $\frac{\sigma(B_c^\pm)\times Br(B_c^\pm \to J/\psi\pi^\pm)}{\sigma(B^\pm)\times Br(B^\pm \to J/\psi K^\pm)}$ and $\frac{Br(B_c^\pm \to J/\psi\pi^\pm\pi^\pm\pi^\mp)}{Br(B_c^\pm \to J/\psi\pi^\pm)}$ at $\sqrt{s} = 7\,\text{TeV}$," CMS PAS BPH-12-011 (2013).

[28] ATLAS Collaboration, "Observation of an Excited $B_c^\pm$ Meson State with the ATLAS Detector," CERN-PH-EP-2014-137 (2014), arXiv:1407.1032[hep-ex].

[29] M. Masetti, F. Sartogo, "Perturbative predictions for B_c meson production in hadronic collisions," Phys. Lett. B, **357** 659 (1995), arXiv:hep-ph/9503491.

[30] I. Gouz, V. Kiselev, A. Likhoded, et al., "Prospects for the B_c Studies at LHCb," Phys. Atom. Nucl., **67** 1559 (2002), arXiv:hep-ph/0211432v1.

[31] S.R. Slabospitsky, "B_c–meson production in hadron–hadron collisions," Phys. Atom. Nucl., **58** 988 (1995).

[32] A. Berezhnoy, A. Likhoded, O. Yushchenko, "Some Features of the Hadronic $B_c^{(*)}$-meson Production at Large p_T," Phys. Atom. Nucl., **59** 709 (1996), arXiv:hep-ph/9504302v2.

[33] C.H. Chang, R.J. Oakes, "Comparative Study of the Hadronic Production of B_c Mesons," Phys. Rev. D, **54** 4344 (1996), arXiv:hep-ph/9602411v1.

[34] ATLAS Collaboration, "Measurement of the differential cross-section of B^+ meson production in pp collisions at $\sqrt{s} = 7\,\text{TeV}$ at ATLAS," JHEP (2013), CERN-PH-EP-2013-089.

[35] K. Nakamura (Particle Data Group), et al., "$J/\psi(1S)$," JPG, **37** 075021 (2010), http://pdg.lbl.gov/2010/listings/rpp2010-list-J-psi-1S.pdf.

[36] CMS Collaboration, "Prompt and non-prompt J/ψ production in pp collisions at $\sqrt{s} = 7\,\text{TeV}$," Eur. Phys. J. C, **71** 1575 (2011), arXiv:1011.4193[hep-ex].

[37] S. Godfrey, "Spectroscopy of B_c Mesons in the Relativized Quark Model," Phys. Rev. D, **70** 54017 (2004), arXiv:hep-ph/0406228v3.

[38] V. Kiselev, "Decays of the B_c meson," arXiv:hep-ph/0308214v1 (2003).

[39] D. Ebert, R. Faustov, V. Galkin, "Weak decays of the B_c meson to charmonium and D mesons in the relativistic quark model," arXiv:hep-ph/0306306v2 (2003).

[40] A. Anisimov, P. Kulikov, I. Narodetskii, K. Ter-Martigosyan, "Exclusive and Inclusive Decays of the B_c Meson in the Light-Front ISGW Model," Phys. Atom. Nucl., **62** 1739 (1999), arXiv:hep-ph/9809249v1.

[41] A. Likhoded, A. Luchinsky, "Light hadron production in $B_c \to J/\psi X$ decays," Phys. Rev. D, **81** 014015 (2010), arXiv:0910.3089.

[42] ATLAS Collaboration, "Performance of the ATLAS Inner Detector Track and Vertex Reconstruction in the High Pile-Up LHC Environment," (2012), ATLAS-CONF-2012-042.

[43] ATLAS Muon Combined Performance Working Group, *Guidelines for Analyses of 2012 Data*, https://twiki.cern.ch/twiki/bin/view/AtlasProtected/MCPAnalysisGuidelinesData2012 (May 2014).

[44] J. Beringer et al. (Particle Data Group), "$B_c^{\pm}$," Phys. Rev.D, **86** 10001 (2014), http://pdg8.lbl.gov/rpp2013v2/pdgLive/Particle.action?node=S091.

[45] ATLAS Collaboration, "Updated Luminosity Determination in pp Collisions at 7 TeV using the ATLAS Detector," (2011), ATLAS-CONF-2011-116.

[46] ATLAS Collaboration, "Observation of the B_d^0 and B_s^0 mesons in the decays $B_d^0 \to J/\psi K^{*0}$ and $B_s^0 \to J/\psi\phi$ in ATLAS," (2011), ATLAS-CONF-2011-050.

[47] ATLAS Collaboration, "Charged-particle multiplicities in pp interaction measured with the ATLAS detector at LHC," New J. Phys., **13** 053033 (2011), arXiv:1012.5104.

[48] M. Paterno, *Calculating Efficiencies and Their Uncertainties*, Fermilab (2004), FERMILAB-TM-2286-CD.

[49] D. Casadei, "Estimating the selection efficiency," JINST, **7** 8021 (2012), arXiv:0908.0130v8.

[50] http://bigscience.web.cern.ch/bigscience/en/lhc/lhc2.html (December 2013).

[51] www.atlas.ch/photos (March 2014).

D Acknowledgements

I would like to thank everyone who supported me in preparing this thesis.

First of all I would like to thank the two persons without whom this project would not have taken place: Prof. Dr. Hans-Christian Schultz-Coulon and Prof. Dr. Sally Seidel. They gave me the opportunity to work on this interesting topic and get an insight to high energy physics research with the ATLAS experiment.

Special thanks belongs to the people at the University of New Mexico where this research was conducted.

- Prof. Dr. Sally Seidel has given me scientific guidance throughout the project. She supported the development with many helpful comments. I was able to learn a lot from her about research at ATLAS. I also have been able to improve my skills in writing a scientific text in English with the help of her comments on my manuscript and my Paper draft. She also volunteered to write the second report on my thesis.

- Dr. Konstantin Toms is the group's representative at CERN. He has a lot of expertise from previous similar analyses and has given me technical guidance. I want to acknowledge his advisement and support during my project. He helped to resolve many coding issues and answered questions on the physics processes. He also provided me with the estimation for the systematic uncertainty of the event counting. Visiting him at CERN allowed me to resolve the last remaining issues.

- Dr. Rui Wang provided me with some example codes and instructions to use them. Most important, she provided me with the analysis code, the skimming code, a code for applying cuts and the fitting of the B^+ invariant mass. She allowed me to use her data-ntuples for the 2012 data in my analysis. With her expertise working with the detection of the $B_c(2S)$ state, she was able to give me valuable advice.

- I also want to acknowledge the support of Aaron Taylor. He helped me to deal with some coding issues and showed me how to calculate the integrated luminosities.

- Special thanks to Prof. Dr. Igor V. Gorelov who helped with some root and RooFit problems. He also gave many helpful comments during group meetings.

- Further members of the research group of Prof. Dr. Seidel are Dr. Prabhakar Palni, Martin R. Hoeferkamp, Haley McDuff, and Neil McFadden. I want to acknowledge their contributions at group meetings, and their comments. I also would like to thank the new group member Aidan Grummer for not giving me a hard time.

Thank you!

Further acknowledgment belongs to the participants of the $B \to J/\psi$ subgroup meetings for their comments. Special thanks go to the conveners: Dr. Daniel Scheirich and Dr. Alastair Dewhurst. They supported me together with Dr. James Catmore to find the right configurations to run the analysis code on Monte Carlo samples. Thank you!

I would like to express my gratitude to Dr. Ioannis Nomidis. He answered some questions on his measurement of the B^+ production cross section with ATLAS and also had some advice for our research. Thank you!

Prof. Dr. Wolfgang Walkowiak answered some questions on the calculation of the efficiencies. Thank you!

I would like to thank the team around Prof. Dr. Schultz-Coulon. They helped me with a lot of paper work and to get the necessary ATLAS and grid credentials. Especially: Prof. Dr. Schultz-Coulon, Dr. Rainer Stamen, and Petra Pfeifer. Thank you!

Many thanks also to the Auslandsamt of the University of Heidelberg and the Global Education Office of the University of New Mexico for supporting the exchange between the two universities, making me an official representative of the University of Heidelberg abroad, and helping me out with questions about visa and residence permit... Thank you!

Last but not least, dear anonymous people of the internet: Thank you for making similar programming issues public online and discussing possible (and impossible) solutions!

Erklärung:

Ich versichere, dass ich diese Arbeit selbstständig verfasst habe und keine anderen als die angegebenen Quellen und Hilfsmittel benutzt habe.

Heidelberg, den 1. September 2014 .....